

Higher Order Optical Magnetic Modes in Dynamic Metamolecules

Omar Ibrahim,^{*,†} Sunghee Lee,[‡] Connor Woods,[†] So-Jung Park,[‡] and Zahra
Fakhraai^{*,†}

[†]*Department of Chemistry, University of Pennsylvania*

[‡]*Department of Chemistry and Nanoscience, Ewha Womans University*

E-mail: omaribr@sas.upenn.edu; fakhraai@sas.upenn.edu

Abstract

Dynamic metamolecules (DMMs) are composed of a dielectric core made of hydrogel surrounded by plasmonic beads that display magnetic resonances when excited by light at optical frequencies. Their optical properties can be controlled by controlling their core diameter by varying temperature. We have recently shown that DMMs display strong optical magnetism, including magnetic dipole and magnetic quadrupole resonances, offering significant potential for novel applications. Here, we use a T-matrix approach to characterize the high order magnetic modes of model metamolecules and confirm the presence of these modes in experiments. We show that higher order modes become prominent as the bead size and the overall structure size grows larger, and when the core size or the inter-bead distance is decreased. We also show that in this limit, mode mixing among these higher order magnetic modes becomes significant in the directional scattering spectrum. We discuss trends in magnetic modes observed in both experiments and simulations and provide suggestions for experimental design and verification of high-order optical magnetic resonances. We demonstrate that the an-

gular scattering of higher-order magnetic modes display Fano-like interference patterns that should be experimentally detectable.

Introduction

There has recently been significant interest in magnetic resonances at optical frequencies for their potential to produce materials with unique optical properties.¹⁻³ Some exciting applications include creating materials with near-zero⁴ or negative^{5,6} refractive indices which can be used in optical cloaking,⁷ tuning of antennae chirality,⁸ making high quality sensors,⁹ and sub diffraction microscopy.¹⁰ A specific subclass of these materials, named magnetic metamolecules, consist of tightly packed clusters of plasmonic nanoparticles (beads) around a dielectric core. These metamolecules have seen great interest in recent years due to their ease of synthesis, tunability, and potent magnetic resonances.¹¹⁻¹³ We have recently demonstrated that the magnetic resonance of these metamolecules can be dynamically controlled using hydrogel cores that can change their core size upon heating (which we call dynamic metamolecules or DMMs).¹² DMMs have been shown to produce experimentally realizable magnetic dipoles and even quadrupoles in solution phase, even in ensemble measurements in both gold and silver, and their properties can be controlled by adjusting the temperature of the solution.¹² This is significant, as tunable higher order magnetic modes display unique scattering behaviors¹⁴ that could serve to further expand the range of applications these systems can provide.

While previous studies have explored the optical behavior of magnetic metamolecules, the majority of these studies have focused on magnetic dipolar resonances, which is deemed experimentally more realizable. However, some recent studies have investigated higher order modes^{13,15,16} but many details remain poorly understood. In particular, a direct connection between theoretical predictions and experimental observations of these higher order modes have not been made and a clear recipe to experimentally realize and verify these modes have not been provided. Here, we fully characterize the scattering behavior of model MMs using a T-matrix approach based on finite-difference time domain (FDTD) simulations. The T-matrix approach is especially powerful compared to standard basis decomposition techniques as it allows us to visualize not only the contribution of each scattering mode but also the influence of each submode and the mode-mixing. Through a single T-matrix calculation, we can obtain this information at any orientation of incident and scattered light.¹⁷ We demonstrate the emergence of higher order magnetic modes as the bead size or the overall structure size grows and demonstrate the potential significance of mode mixing in the differential scattering and total scattering cross sections, which has not been explored in previous studies. We also characterize the angular scattering of our model systems and show how the higher order modes can interfere to produce Fano-like resonances in certain directions which can be used as a strategy to experimentally observe higher order modes. Using this concept we use backscattering analysis to propose a method to detect the magnetic octupole in the far field, which has not been previously identified or experimentally observed.

We compare these results with experimental data that show magnetic quadrupoles. We demonstrate evidence of mode mixing between magnetic modes and show the conditions under which this becomes visible. Our results provide a recipe for accurately identifying the magnetic quadruple and octupole modes using comparisons between forward and backward scattering experiments.

Methods

Experimental Methods

Fabrication of Gold DMMs. Gold DMMs were fabricated by following a previous literature procedure.¹² Freshly prepared gold nanobead solution dispersed in 1 mM sodium citrate solution (4 mL) and 10 μ L of 1 wt% poly(N-isopropylacrylamide) (PNIPAM) hydrogel solution were mixed in a 10 mL glass vial. The concentration of gold nanobead solution and other structural parameters are summarized in Table S2. This solution was kept undisturbed at room temperature for about 12 h. As DMMs are heavy, they settle to the

bottom of the vial over time, while unattached nanobeads remain in the supernatant. The supernatant was removed, the precipitate was redispersed in 1 mM sodium citrate solution (4 mL), followed by sonication for 10 s. gold DMMs were characterized using scanning electron microscope (SEM, JEOL JSM-7610F at an accelerating voltage of 15 kV).

Temperature-dependent extinction measurement. Temperature dependent extinction spectra of gold DMMs were recorded with an Agilent 8453 UV-Vis spectrometer. For this, gold DMMs solution (3 mL) were taken in a cuvette (dimensions (H×W×D): 45×12.5×12.5 mm³, optical path length: 10 mm) and the extinction spectra were measured by increasing the temperature at the rate of 1°C per min from 20 to 55°C under magnetic stirring. Samples were equilibrated for 1 min at each temperature.

Simulated MMs

To generate model metamolecules (MMs), points were randomly distributed on a unit sphere. A Monte Carlo method (with $T = 0$ K) was then used to uniformly separate the points by treating them as point charges. These structures were then scaled up and imported into Lumerical FDTD Solutions where optical properties of the structure could be determined (see our previous publication for details¹²). The T-matrix method described by Hastings et. al.¹⁷ was adopted, where both the incident field and the scattered field were expanded into vector spherical harmonic basis functions at many random orientations. This provides an over-determined set of equations, which were then numerically solved to obtain the T-Matrix. This T-Matrix can then be used to characterize the complete scattering properties of the MMs for any orientations of incident and scattered light.

FDTD Simulations

The structures generated by the Monte Carlo method were imported into Lumerical FDTD Solutions Software. Each point charge was replaced by a gold spherical bead with optical properties based on the CRC Handbook of Chemistry and Physics.¹⁸ The core index was set to 1.56 to mimic the hydrogel index of refraction for DMMs and a background index of 1.333 was used to model the fact that the experimental DMMs are measured in aqueous solutions.¹² See Table S1 for all structural parameters for MMs and DMMs used in this study.

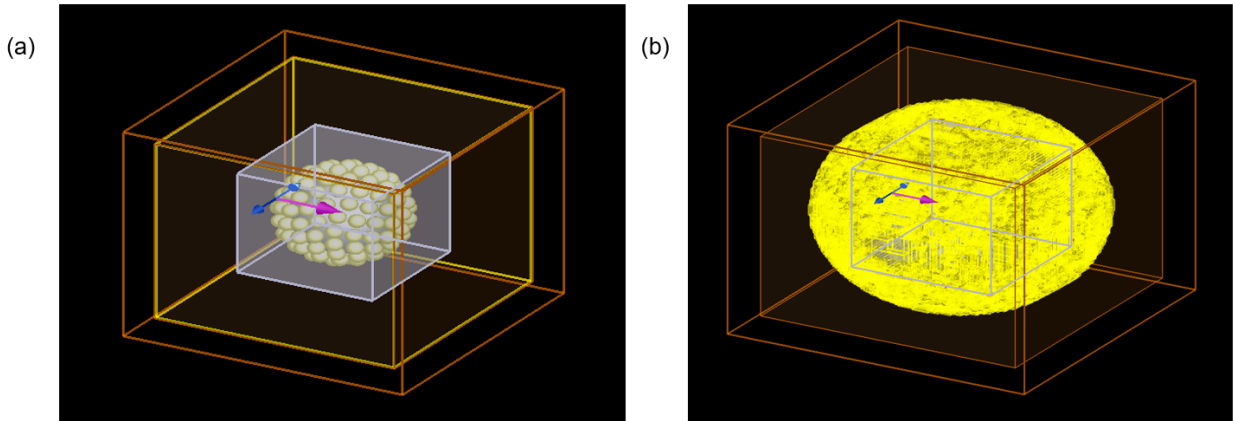


Figure 1: Simulation region as seen in Lumerical FDTD package with (a) the cubic field monitor and (b) the cubic shell field monitors. The grey box represents Lumerical’s built-in TFSF source and the yellow boxes represent the field monitors.

To distinguish between the incident light and scattered light in our simulations Lumerical’s built-in TFSF (total-field scattered field) source was used. This source specifies a box whereby a plane wave is

introduced on one side and subtracted on the other. This has the effect of separating the region into a total field region and a scattered field region.¹⁷ It is in this scattered field region where the \vec{E} field and \vec{H} fields can be measured in a cubic box (Figure 1a) and these fields can then be interpolated to our spherical shell of interest to calculate the T-matrix. To ensure that none of the incident field is contained in this sphere the TFSF source must be completely inscribed in our sphere of interest which requires that the field monitors be at least a factor of $\sqrt{3}$ from the edge of the TFSF source. In this work, instead of saving the entire inscribing sphere as has been done in our previous works,¹⁷ we use many cubic monitors to construct a thin shell about the radius of interest as shown in Figure 1b (details of this approach are in SI). This approach reduces the requirements for disk space, allowing simulations on larger systems.

Throughout this paper T-matrix results are also compared to the scattering cross section and the differential scattering cross section outputted directly by Lumerical FDTD as a benchmark. To obtain the scattering cross sections, the MM is surrounded by a box composed of six plane power monitors that when factored in together gives the total power scattered by the model MM. To obtain the differential scattering cross sections, the far field projection feature offered by Lumerical FDTD was used.

T-Matrix Calculations

The incident field ($\vec{E}_i(\vec{r})$), which is a plane polarized wave here, within a circumscribing sphere and the scattered field ($\vec{E}_s(\vec{r})$) outside a circumscribing sphere can be written as infinite linear combinations of spherical waves as:

$$\vec{E}_i(\vec{r}) = \sum_{n=1}^{\infty} \sum_{m=-n}^n [a_{mn}^M(kr, \theta, \phi) Rg\vec{M} + a_{mn}^N Rg\vec{N}(kr, \theta, \phi)] \quad (1)$$

$$\vec{E}_s(\vec{r}) = \sum_{n=1}^{\infty} \sum_{m=-n}^n [b_{mn}^M \vec{M}(kr, \theta, \phi) + b_{mn}^N \vec{N}(kr, \theta, \phi)] \quad (2)$$

where \vec{M} and \vec{N} in equations 1 & 2 constitute a complete basis and $Rg\vec{M}$ and $Rg\vec{N}$ are regularized to contain no singularity within the sphere. Note that \vec{M} and $Rg\vec{M}$ represent the electric field due to magnetic modes and \vec{N} and $Rg\vec{N}$ represents the electric field due to electric modes. n represents the mode order (monopole, dipole, etc.) while m represents the given sub-mode, $-n \leq m \leq n$. $\{a\}_{mn}$ and $\{b\}_{mn}$ are the basis coefficients of the incident and scattered waves respectively while the superscript N and M denote the electric and magnetic components respectively. Due to the linearity of Maxwell's equations and their boundary conditions,¹⁹ the incident and scattered fields are linearly related through the T-matrix ($\overline{\overline{T}}$):

$$\begin{bmatrix} \vec{b}_{mn}^N \\ \vec{b}_{mn}^M \end{bmatrix} = \overline{\overline{T}} \begin{bmatrix} \vec{a}_{mn}^N \\ \vec{a}_{mn}^M \end{bmatrix} \quad (3)$$

$$\overline{\overline{T}} = \begin{bmatrix} \overline{\overline{T}}^{EE} & \overline{\overline{T}}^{EM} \\ \overline{\overline{T}}^{ME} & \overline{\overline{T}}^{MM} \end{bmatrix} \quad (4)$$

Here $\overline{\overline{T}}^{EE}$ is the sub-matrix that gives the electric influence on the scattered field while $\overline{\overline{T}}^{MM}$ is the sub-matrix that gives the magnetic influence on the scattered field. However, we note that all T-matrix calculations here are performed only on the electric field of light as indicated in equations 1 & 2. $\overline{\overline{T}}^{EM}$ and $\overline{\overline{T}}^{ME}$ are the sub-matrices that provide electric-magnetic mode mixing. It is important to note that $\overline{\overline{T}}$ and its sub-matrices are infinite matrices and thus they must be truncated at a given mode. Here, we use up to $n = 4$, which corresponds to hexadecapole modes. a_{mn}^M and a_{mn}^N can be directly calculated for a plane wave propagating in any direction. To determine b_{mn}^M and b_{mn}^N we obtain \vec{E} and \vec{H} at every point within a shell surrounding the particle and outside the TFSF source. We then define a sphere within this shell to which \vec{E}_s and \vec{H}_s can be interpolated and write:

$$b_{mn}^M = \frac{i}{c\epsilon_0 N} \frac{[\oint (\hat{r} \cdot \vec{H}_s) Y_n^{-m}(\theta, \phi) dA] k(2n+1)}{4\pi r_0^2 \gamma_{mn} (-1)^m n(n+1) h_n(kr_0)} \quad (5)$$

$$b_{mn}^N = \frac{[\oint (\hat{r} \cdot \vec{E}_s) Y_n^{-m}(\theta, \phi) dA] k(2n+1)}{4\pi r_0^2 \gamma_{mn} (-1)^m n(n+1) h_n(kr_0)} \quad (6)$$

where r_0 is the radius of the integration sphere, N is the refractive index, and $\gamma_{mn} \equiv \sqrt{\frac{(2n+1)(n-m)!}{4\pi n(n+1)(n+m)!}}$.^{17,20} Note that in these simulations rather than rotating the incident light we instead for convenience choose to rotate the structure. If a_{mn}^M , a_{mn}^N , b_{mn}^M , and b_{mn}^N are determined for k different random orientations of incident light, we can write:

$$\begin{bmatrix} b_{mn}^{N,1} & b_{mn}^{N,2} & \dots & b_{mn}^{N,k} \\ b_{mn}^{M,1} & b_{mn}^{M,2} & \dots & b_{mn}^{M,k} \end{bmatrix} = \overline{\overline{T}} \begin{bmatrix} a_{mn}^{N,1} & a_{mn}^{N,2} & \dots & a_{mn}^{N,k} \\ a_{mn}^{M,1} & a_{mn}^{M,2} & \dots & a_{mn}^{M,k} \end{bmatrix} \quad (7)$$

To compute the T-matrix from the above expression we do a minimization over the T-matrix elements using the objective function $\|\overline{\overline{TA}} - \overline{\overline{B}}\|_F^2$ (where the subscript F denotes the Frobenius norm). In this regression we take advantage of the reciprocity relation $T_{-m'n'(-m)n}^{ij} = (-1)^{m'+m} T_{mnm'n'}^{ji}$ for $i, j = \{E, M\}$, cutting the number of free parameters by a factor of almost 2.²¹ A possible set of free parameters implied by this reciprocity relation can be visualized in Figure S2 of SI.

This approach is advantageous as it allows for the T-Matrix of a large number of frequencies to be determined simultaneously whereas traditionally the T-matrix is calculated separately for each desired frequency. Since we only require the fields scattered in any sphere about the scattering body his approach is also highly robust to sharp features.¹⁷ Once we calculate the T-matrix for each desired frequency all desired optical properties can be determined from it. In particular, from the T-matrix we obtain the scattering amplitude dyad $\overline{\overline{F}}$ from which numerous parameters of interest are obtained. Relevant parameters derived from $\overline{\overline{F}}$ include \vec{E}_s and \vec{J}_D , the far field scattered field, and the far field displacement current at all points. We also obtain $\vec{X}(\theta, \phi)$, the vector scattering amplitude, which we take to be $\vec{X} = \overline{\overline{F}} \cdot \hat{\beta}$ (where $\hat{\beta}$ is the polarization vector) such that in the far field, $\vec{X} \cdot \hat{\beta} = 0$ and $\vec{E}_s = \frac{e^{ikr}}{r} \vec{X}$. Finally we also derive the scattering cross section C_{scat} and the differential scattering cross section $\frac{dC_{scat}}{d\Omega}$ for any given direction. To see the details of how these are obtained from the T-matrix see section SIIL.^{19,21}

Results

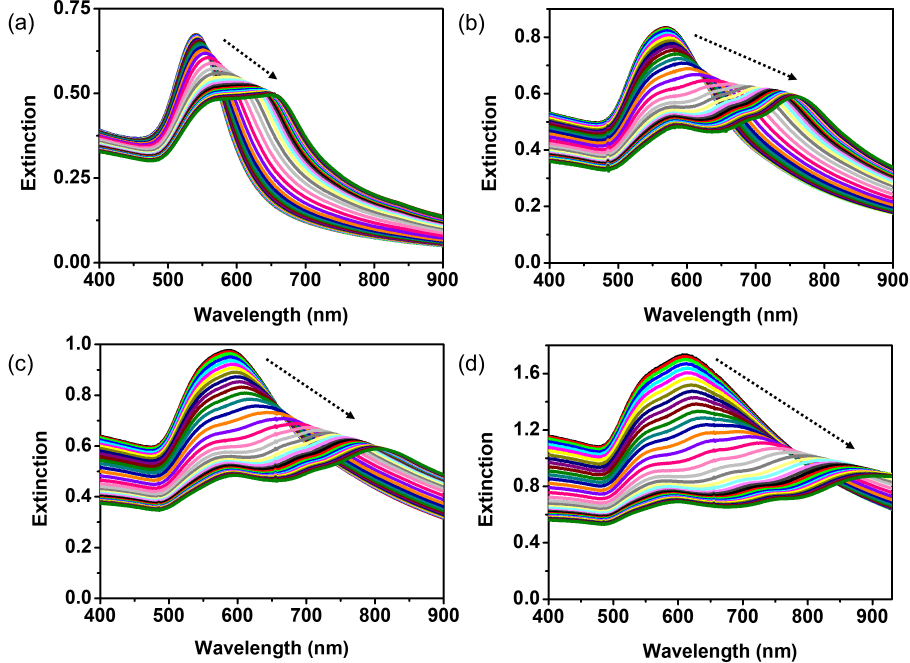


Figure 2: (a-d) Temperature-dependent experimental extinction spectra of gold DMMs with nanobeads of average number and size (a) $N = 57 \pm 3, D = 35 \pm 3$ nm, (b) $N = 61 \pm 4, D = 45 \pm 2$ nm (c) $N = 59 \pm 4, D = 49 \pm 2$ nm, and (d) $N = 41 \pm 4, D = 60 \pm 3$ nm. Other structural parameters are summarized in Table S2. The dashed arrow in the inset of spectra shows the direction of increasing temperature from 20 to 55°C, resulting in shrinking values of the core diameter, Z .

We have previously reported experimental and FDTD simulation data for DMMs, where we demonstrated the emergence of an electric dipole mode and a magnetic dipole mode upon heating the DMMs above the LCST (lower critical solution temperature) of the hydrogel core.¹² However, we also saw additional peaks rise as the structures grew larger which we hypothesized were due to higher order magnetic modes. In this work we have performed a similar set of experiments using larger gold nanobeads to further investigate this trend and study the origin and details of these higher order modes. We show these results in Figure 2. Each subfigure corresponds to heating a solution of DMMs with differing nano bead sizes (D), with D increasing from Figure 2a to 2d. As we increase the temperature, the hydrogel core diameter (Z) shrinks, making tighter packings of the beads, and thus increasing the strengths of the emergent modes. We note that the core size at the maximum temperature is likely larger for larger bead sizes, since the core is not able to shrink as much due to increased packing frustration of the beads. For each D , as we increase the temperature, decreasing Z and therefore the interbead distance (d), a prominent middle peak emerges. This effect is more prominent at larger D (Figure 2 c & d). In order to better understand the nature and the rise of these plasmon resonances (which is important to understanding how to experimentally tune them), we simulate various structures and compute the T-matrix in order to visualize the modal contributions to each of the peak features.

We first focus our attention to one specific structure; a simulated MM with $N = 126$ number of beads with $D = 70$ nm, placed on a dielectric core with diameter, $Z = 415$ nm. A histogram of inter-bead distances (d) is shown in Figure S4. We chose this structure because it has strong resonances with the most number of higher-order magnetic modes active, while still being computationally tractable. We will make references to other structures where relevant. This structure is shown in the inset of Figure 3. We have computed

the T-matrix for this structure at 40 different wavelengths and have decomposed the scattering cross section into its individual modes. (Figure 3). To calculate the T-matrix, we chose the T-matrix order $n = 4$, which includes modes up to the electric and magnetic hexadecapoles, assuming that the contribution from higher order modes are negligible.

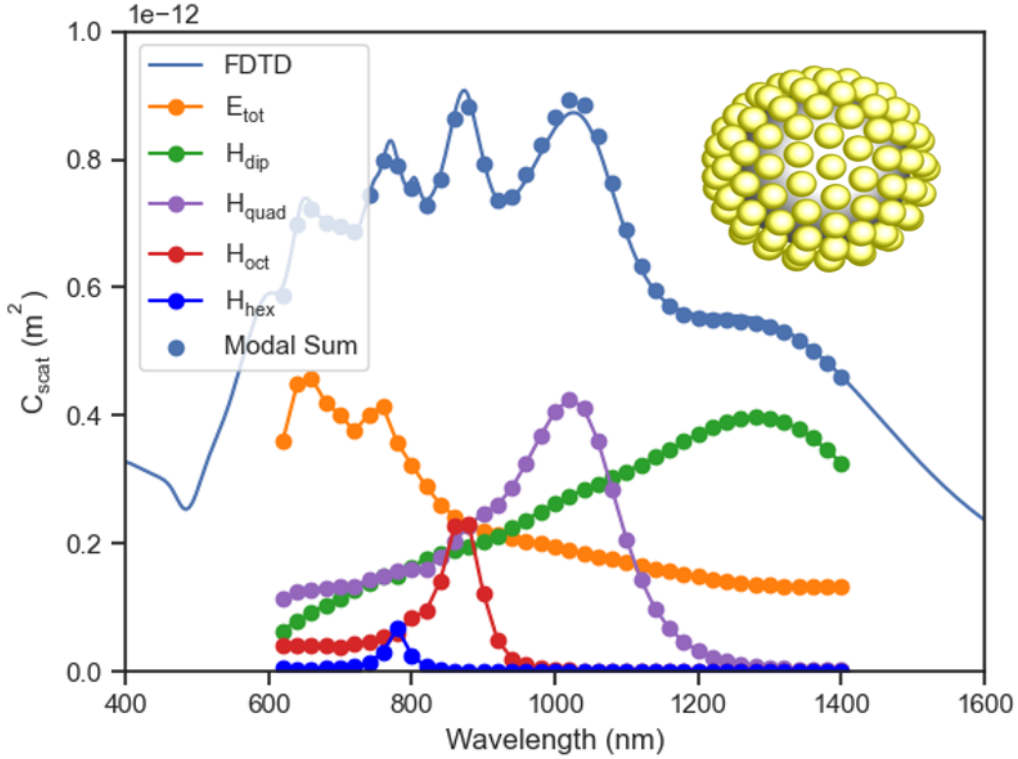


Figure 3: Scattering cross section (C_{scat}), calculated based on the full T-matrix ($n = 4$), along with its relevant modal contributions; the sum of all electric modes (E_{tot}), magnetic dipole (H_D), magnetic quadrupole (H_Q), magnetic octupole (H_O), and magnetic hexadecapole (H_H) modes, for a $Z = 415$ nm diameter MM with $N = 126$ gold beads of $D = 70$ nm diameter. The solid line is the total scattering cross section directly obtained from FDTD simulations. The simulated structure is shown in the inset.

As we can see, the sum of the scattering cross sections of each mode sum up to the FDTD results demonstrating the validity of our approach. We see that using $n = 4$ captures all of the observed resonances in the structure so there is no need to add more modes which would increase the dimensionality of our T matrix by 22 and possibly lead to over-fitting. Moreover, we see that magnetic resonances dominate the spectrum, particularly at long wavelengths ($\lambda > 780$ nm) where the contribution from the electric modes slowly decays. Surprisingly, the stronger resonances originate from higher order magnetic (quadrupole and octupolar) modes throughout most of the spectrum. The electric modes are significant yet very broad throughout the entire spectrum except at low wavelengths. As such, each peak in the total scattering above $\lambda = 780$ nm to correspond to a magnetic, rather than an electric mode.

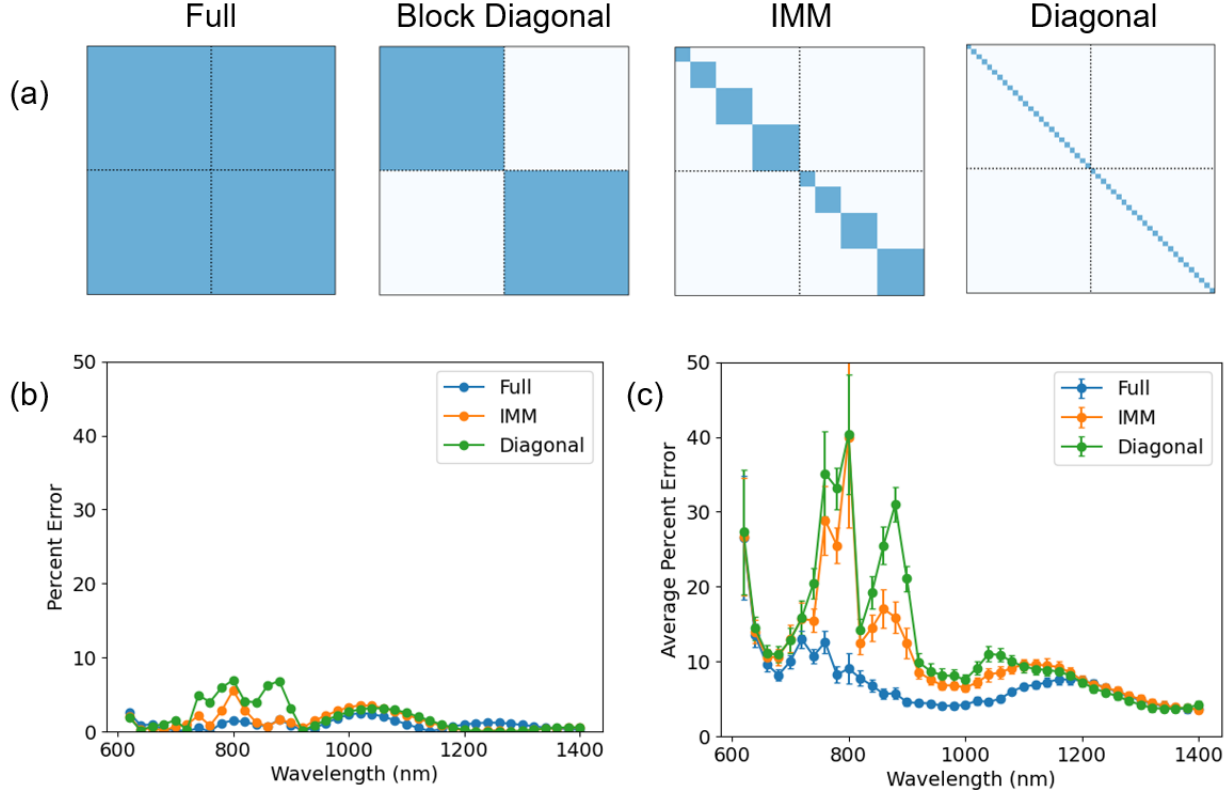


Figure 4: Various types of T-Matrices. Non-zero components (used to fit) are highlighted with dark blue and zero components (not fitted) are highlighted with light blue. (a) From left to right: full T-matrix, block diagonal with all the electric and magnetic modes mixed (not further studied in this paper), independent mode mixing T-matrix (where modes with the same order n are mixed), and Diagonal. (b) Error of each T-matrix compared to FDTD results for C_{scat} . (c) The average of the errors for 100 different orientations of differential scattering cross section (with error bars as the standard error)

The data in Figure 3 represent the full T-matrix fitting. However, it may not always necessarily to fit the full T-matrix and the full fitting may result in over-fitting. To investigate whether the full T-matrix is needed here, we explore three different T Matrices; diagonal, independent mode mixing, and full. We have excluded a fourth possible T-matrix, a block diagonal one (schematically shown in Figure 4a), because large differences between this T-matrix and the full T-matrix implies significant electric-magnetic interference, requiring strongly chiral structures,²⁰ which is not the case here. A graphical representation of the nonzero terms for these matrices can be seen in Figure 4a. A diagonal T-matrix would imply that there is no mode mixing (meaning that all submodes that enter contribute only to the scattering of that submode), while an IMM T-matrix implies that all entering modes can only mix among their respective submodes. To evaluate the performance of these fits, we computed the scattering cross section for the structure and plot the error as a function of wavelength for each T-matrix (Figure 4b). We also computed the differential scattering cross section for an incident plane wave at 100 random orientations and plotted the mean error compared to FDTD results as a function of wavelength (Figure 4c).

The results indicate that both the diagonal and IMM T-matrices produce significant errors in predicting the higher order octupole and hexacecapole resonances, though in the case of the IMM T-matrix, this error only manifests itself in the accuracy of the differential scattering cross sections. These results mean that there is indeed mode mixing between various order modes and that the full T-matrix includes key details of the scattering behavior of the magnetic modes of interest, especially at the octupole and hexadecapole modes which we will discuss in more details below. As such, we opt to use the full T-matrix calculations for the data shown hereon.

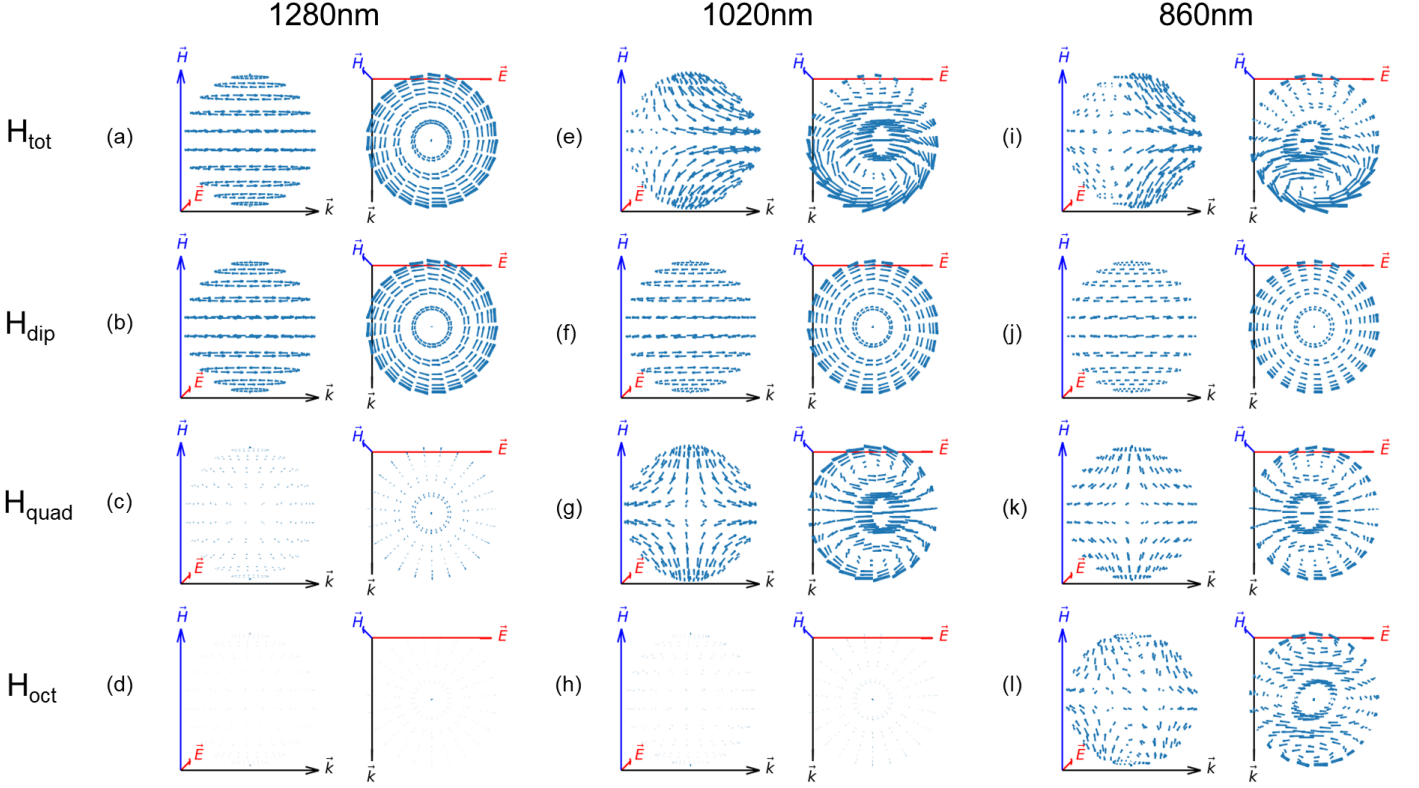


Figure 5: Far field displacement currents contributing to the total magnetic field (H_{tot} , top row) as well as the break down for each individual magnetic mode (rows 2-4), at the (a-d) magnetic dipole resonance (1280 nm), (e-h) magnetic quadrupole resonance (1020 nm), and (i-l) magnetic octupole resonance (860 nm). In each case from top to bottom we show total magnetic resonance, magnetic dipole resonance, magnetic quadrupole resonance, and magnetic octupole resonance to view the modal contributions to the current. For each condition the figure on the left shows the plane of \vec{H} and \vec{k} (side view) and the figure on the right shows the plane of \vec{E} and \vec{k} (top view)

Using the full T-matrix we look at the far field displacement current plots (Figure 5) which can provide insight into the spatial distribution of various modes based on their displacement currents circulating between the beads (see section SIII for details on the calculation). As shown in Figure 5, at long wavelengths, close to the magnetic dipole resonance ($\lambda = 1280$ nm) we observe a magnetic dipole resonance exists which is due to the formation of a global loop of induced displacement currents circulating throughout the entire structure (Figure 5 a&b). This observation is consistent with previous predictions^{15 22 23} and experimental works^{11, 24}

At this wavelength, the contribution from the magnetic quadrupole and octupole modes are negligible. We see that as the wavelength decreases, the currents become more and more phase lagged across the structure, resulting in the emergence of a second current loop. This manifests itself through the strengthening of the quadrupole mode, which is super-imposed on a weakening dipole mode (Figure 5 e-h). We see that at the quadrupole resonance ($\lambda = 1020$ nm) the magnetic dipole is in phase with the magnetic quadrupole resulting in enhanced forward scattering and weakened backscattering. The magnetic octupole mode remains weak at these wavelengths. As we continue to decrease the wavelength, three loops of current emerge. The loops at the top and bottom of the structure are out of phase with the central loop, generating magnetic octupole resonance at $\lambda = 860$ nm. These currents cannot be trivially described through a linear combination of magnetic dipole modes and magnetic quadrupole modes. Overall, the larger the structure, the more we observe a phase lag between currents at various positions across the structure, which results in the vertical stacking of various magnetic dipole modes, resulting in the emergence of higher order magnetic modes that dominate the spectrum.

Discussions

Exploring the Properties of Higher Order Magnetic Modes

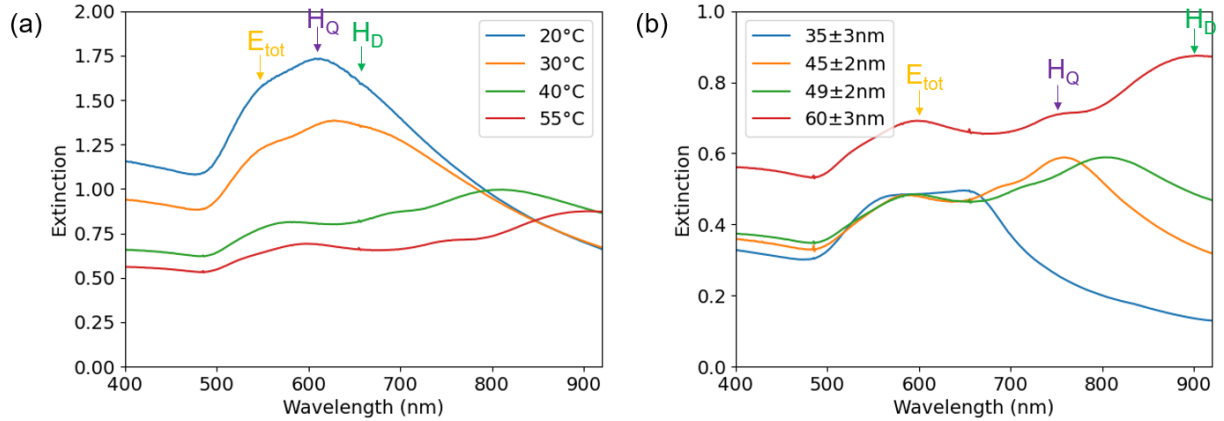


Figure 6: (a) Experimental extinction spectra of gold DMMS with beads of average size $D = 60.0 \pm 3$ nm at various temperatures, and (b) the experimental extinction spectra of gold DMMS for various average bead sizes at 55°C. We identify the origins of observed resonances by comparison with simulation data in Figure 7. The predicted magnetic dipole resonance is marked with " H_D ", the predicted magnetic quadrupole resonance is marked with " H_Q ", and the predicted electric resonance is marked with " E_{tot} ".

In order to highlight the trends of the plasmon resonance frequency shifts, we plot a subset of the experimental data from Figure 2 in Figure 6, showing the wavelength of each peak as a function of both temperature for the the largest structure and bead size, D at 55°C (most compact structures for each D). We observe that both decreasing Z and increasing D result in the emergence of peaks resembling the dipole and quadrupole modes observed in Figure 3. To make a more direct comparison and assignments of these peaks, we simulated structures with similar properties, and calculated their magnetic modes by performing a basis decomposition of FDTD data, which stops short of calculating the full T matrix but still allows us to see the modal scattering strength for the simulated orientation (Figure 7).

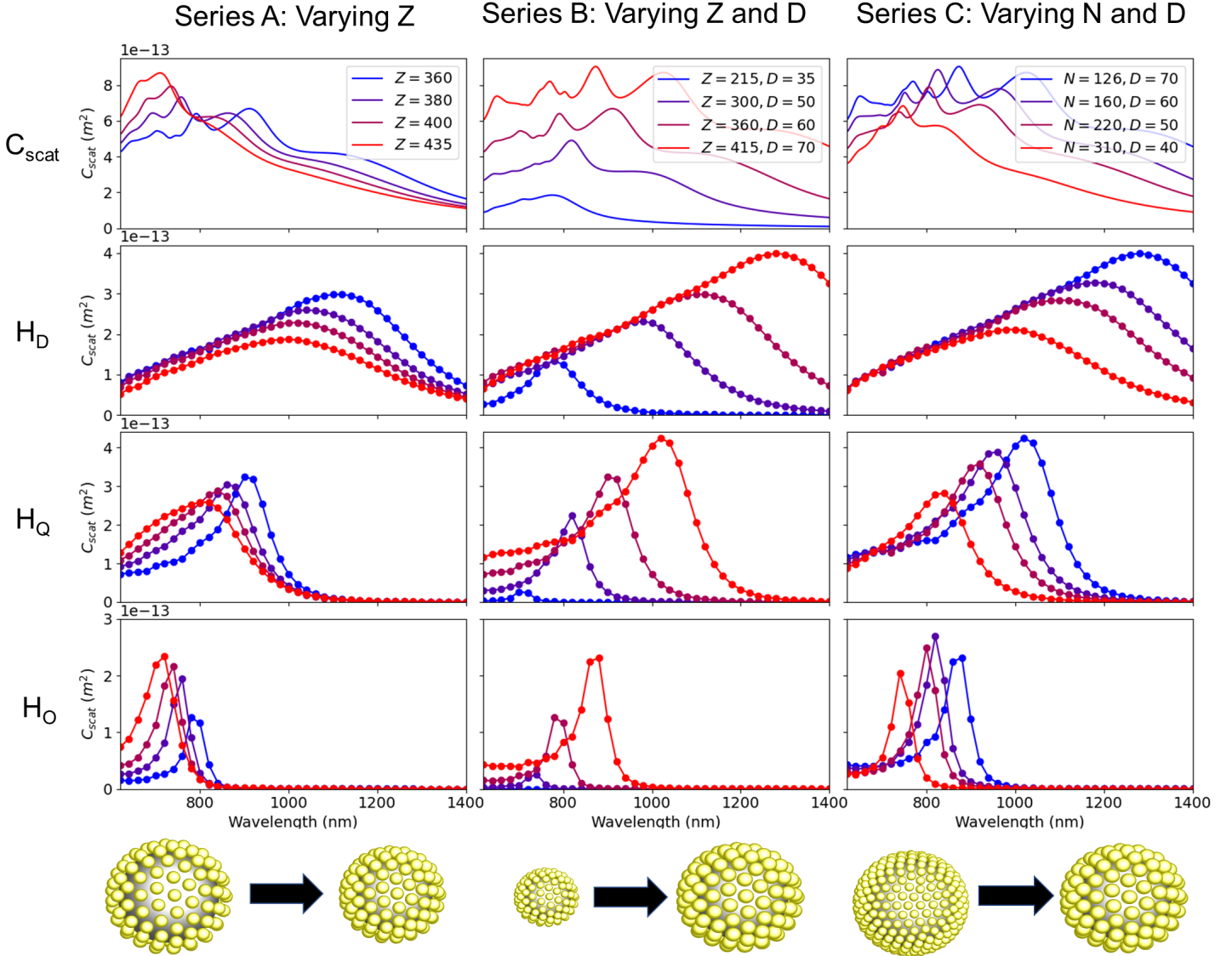


Figure 7: Simulations exploring trends for simulated MMs. We show the total FDTD scattering and computed magnetic dipole, magnetic quadrupole, and magnetic octupole scattering cross sections for (A) a series with $N = 126, D = 30nm$, and varying Z (corresponding to growing the core without changing the beads); (B) a series with $N = 126$ and varying Z with D (corresponding to scaling up a constant structure); and (C) a series with $Z = 415nm$ and varying N and D (corresponding to increasing and shrinking the number of beads leaving bead density unchanged). The top row of each series gives the total FDTD scattering cross section, the second row gives the computed magnetic dipole scattering cross section, the third row gives the computed magnetic quadrupole scattering cross section, and the fourth row gives the computed magnetic octupole cross section. Structure images from both extremes of each series are included below the figure.

Figure 7a shows the modal break down for the core size, Z (see Figure S6 for full modal breakdown calculations). Thus Figure 7a allows us to identify the experimental resonances seen in Figure 6a. The trend shown overall provides excellent agreement with experiments. As the core size is reduced, the strength of the peak is reduced and broadens forming various weaker peaks, each corresponding to a different magnetic mode. Thus we see that as Z is increased, the magnetic mode resonances broaden and blue-shift leading to an

overlap of the individual modal resonances resulting in one large peak. We can clearly see this phenomenon happening in the experiments as we reduce the temperature in Figure 6a. Thus, it appears that shrinking the core does not induce magnetic modes but rather increases their quality factor and spectrally spreads them allowing them to become more visible. In fact, as the mode order increases, resonances become stronger with core size growth. Overall, we can confidently assign the middle experimental peak in Figure 6a to a magnetic quadrupole resonance and the high-wavelength experimental peak to the magnetic dipole resonance. The low-wavelength peak is likely due to a mixture of electric modes as can be seen in Figure S6 since it shifts minimally with structure size, Z .

In the second data series in Figure 7b we increase the core size Z as well as the bead size D leaving the overall structure constant and the minimum inter bead distance (d) approximately constant (see Figure S7 for full modal breakdown). This most closely corresponds to the series in Figure 6b, since in both cases we have an increase in the bead size and core size as well. This series again provides good agreement with the experimental trends. We see that increasing Z with the same particle density greatly strengthens and red shifts the magnetic modes, with the lower order modes shifting more strongly and the higher order modes eventually overtaking the lower order modes in strength. Here, unlike the previous series, the magnetic peaks red shift with the core size (explained in more details below). Overall, we can again confidently assign the middle peak that emerges in larger experimental structures in Figure 6b to the magnetic quadrupole and the high-wavelength experimental peak that appears in all structures to the magnetic dipole resonance. Again, like in Figure 6a, the low-wavelength peak is likely due to a mixture of electric modes as can be seen in Figure S7 since it shifts minimally with structure size.

We have also simulated a series shown in Figure 7c, where we maintain Z constant, but reduce D and increase N (see Figure S8 for full modal breakdown). We see that as we shrink and increase the number of beads keeping the core size constant, the peaks blue shift similar to growing the core in Figure 7a. Also similar to Figure 7a is the fact that the magnetic quadrupole peak and the magnetic octupole peak strengthen in intensity relative to the magnetic dipole resonance. In fact, at $D = 40nm$, the only significant features visible in the total scattering are the magnetic quadrupole and magnetic octupole modes. Much of the reduction in the intensity comes from the weakening of the magnetic dipole and especially the electric quadrupole and electric octupole (see Figure S8). Unlike in Figure 7a however the peaks still remain distinct in the total scattering since they narrow instead of widen which helps keep them from clumping together. This could overall imply using large core sizes and large numbers of small beads could allow for the generation of DMMs with strong, distinguishable high order magnetic resonances and weak lower order modes (dipole).

A Mie theory based explanation for these observations is the fact that the magnetic component of the incident electric field for a given mode and wavelength peaks at a certain distance from the center of the structure. The resonance becomes narrower and blue shifts as the mode order increases (see Figure S11). The resonance for all modes also broadens and red shifts as we move further from the center of the structure. When the beads fall within this resonant zone for a certain mode, the dipoles within the beads can resonate with the incident magnetic mode leading to strong magnetic scattering. This explains why higher order modes have sharper resonances, and require larger structures or cores with high refractive indices¹⁵ to be excited (see Section SVIII for more details). This also explains why peaks tend to broaden and red shift with larger bead distances from the center.

This explains the results we see in Figures 6 and 7. As the structure is scaled up in series b, the beads move further from the center of the structure resulting in a red-shift in the peak position and broadening of magnetic resonance for a constant structure. However, in both experiments and simulations, we see the opposite trend for series a. In this case, as we grow the structure, while the peaks still widen as expected, the peaks actually blue-shift as opposed to red-shift as we might assume. This is likely due to the fact that the beads become more spread out unlike in series b and so more energy is required to make farther beads resonant. In Figure 7c, we both move the beads closer to the center by shrinking them as well as increase the total amount of interbead space and so this blue-shift is likely a combination of these two discussed factors.

Our simulated results are thus highly consistent with the trends shown in experimental data for large DMMs. In simulations, similar to experiments, we observe that growing the core reduces the spectrum to a single peak, but in contrast to what we hypothesized, the higher order magnetic modes don't significantly weaken but rather collapse together (Figures 6a and 7a). Scaling bead size with core size was shown to be an effective way to excite visible higher order modes in both simulations and experiments (Figures 6b and 7b).

However, using smaller beads for this task (as in Figure 7c) could help enhance higher order modes relative to the lower order modes since we see in simulations that the magnetic dipole and higher order electric modes weaken considerably more than the magnetic quadrupole and octupole while still ensuring the peaks remain distinct.

Mode Mixing in Dynamic Metamolecules

We have seen previously in Figure 3 that the scattering cross section of the diagonal T-matrix deviates significantly from the FDTD results for the higher order octupole and hexadecapole modes. In particular, the diagonal T-matrix underestimates the contribution of both modes (see Figure S12). To visualize the interference terms of the T-matrix that are critical for the accurate description of the structure by the full T-matrix, we visualize the amplitude of the magnetic elements of the full T-matrix elements at the magnetic dipole, magnetic quadrupole, magnetic octupole, and magnetic hexadecapole resonance, as shown below:

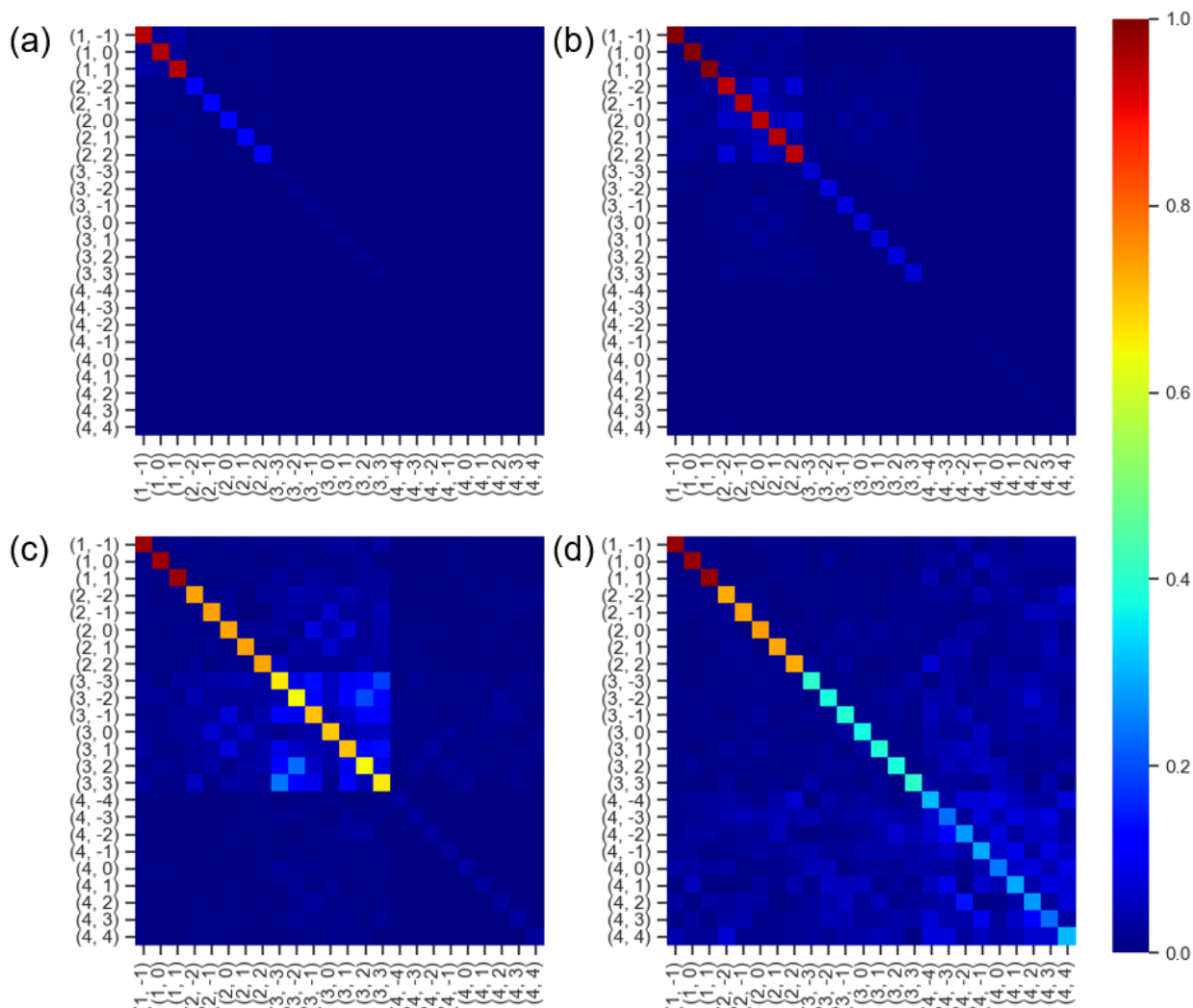


Figure 8: The magnetic elements of the full T-matrix at the magnetic dipole (1280 nm), magnetic quadrupole (1020 nm), magnetic octupole (860 nm), and the magnetic hexadecapole resonance (780 nm). The labels indicate (n, m) where n is the mode order ($n = 1$: dipole, $n = 2$: quadrupole, etc) and m is the submode ($-n \leq m \leq n$)

In Figure 8, we can see that the strength of the mode mixing (off diagonal) terms relative to the diagonal

terms increases as n increases. These terms are especially strong in the case of the magnetic octupole ($n = 3$) and hexadecapole ($n = 4$), with the off diagonal terms of the magnetic octupole and magnetic hexadecapole modes reaching $1/3$ and $1/2$ of the strength of their respective diagonal terms respectively. Both the increase in relative strength of off diagonal terms, and the relative number of terms, compared to the diagonal ensures that the mixing becomes more apparent as the mode order (n) grows. This can be seen as a manifestation of the fact that higher order modes are more localized and thus have more complex currents. As such, it is possible that the polarization currents are more susceptible to distortion by the variations in the local geometry. Interestingly, we see that higher order modes tend to also mix with lower order modes, as seen especially in the case of the octupole and hexadecapole modes. This higher order inter-mode mixing is significant in the directional scattering as seen from the high IMM T-matrix error compared to the full T-matrix error in Figure 3c.

We can further visualize the distortion effect of mode mixing on the scattering behavior and currents of MMs. By zeroing out all rows of the T-matrix except for the mode of interest, and then calculating the scattering amplitude $|\vec{X}(\theta, \phi)|$ from it, we can observe the far field scattering amplitude of individual modes. This is shown in Figures 9a-b where we show radial plots of the the magnitude of the scattering amplitude $|\vec{X}|$ for both a mixed octupole (as calculated through the full T-matrix) and a pure magnetic octupole mode (as calculated through the respective diagonal T-matrix). The plane wave used to excite the structure when decomposed into a sum of spherical waves contains only nonzero amplitude from the $m = -2$, $m = 0$, and $m = 2$ magnetic octupole submodes. Thus if mode mixing is significant we may expect to see scattering from other submodes as well.

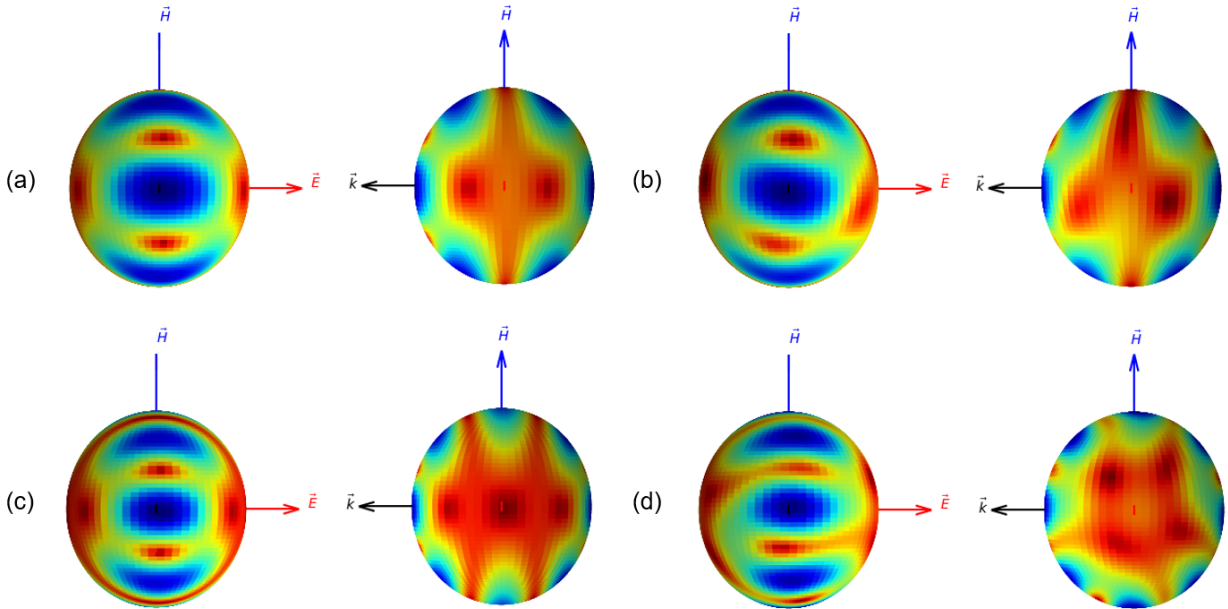


Figure 9: (a & b): Amplitude, $|\vec{X}|$ of the octupole mode at 860 nm (octupole resonance) for (a) a pure magnetic octupole mode and (b) a mixed magnetic octupole mode. $|\vec{X}|$ of the magnetic hexadecapole mode at 780 nm (hexadecapole resonance) for (c) a pure magnetic hexadecapole and (d) a mixed magnetic hexadecapole mode. The blue regions represent areas of high scattering amplitude while the red regions represent areas of low scattering amplitude. The structure used is the one that was used to obtain the spectrum in Figure 3 ($N = 126, D = 70, Z = 415$)

In both cases (Figure 9a-b) we observe the characteristic 6 lobe octupolar scattering pattern. However, in the mixed case (Figure 9b) we clearly see that the modes are distorted. Thus, though the plane wave exciting the structure only contains nonzero amplitude from the $m = -2$, $m = 0$, and $m = 2$ octupole submodes, we can still visually observe active albeit weak currents from all other octupolar modes. These

results are even more pronounced in the case of the magnetic hexadecapole (Figure 7c-d). It is likely that the randomness of the structure contributes to this distortion effect as we have previously shown that mode mixing can be significant in disordered, asymmetric optical systems like spiky nanoshells.¹⁷ We also note that while the pure modes are relatively symmetric and achiral, the distortion from the mixed modes breaks this symmetry causing the scattering pattern to gain a slight amount of chirality which can be potentially useful for various applications. Overall, these observations imply that mode mixing can potentially bring about or enhance chiral modes within MMs.

Mode mixing effects are not too significant in the total scattering but may have significant implications for experiments involving more selective excitations. A single plane wave excites submodes from all modes so the effect of mode mixing is not seen too much since we have shown that only higher order modes have stronger mode mixing effects. However, experiments that use specialized polarizations to enhance higher order modes may see enhanced mode mixing phenomena. To simulate single mode excitations we can hand pick a set of incident coefficients and then apply the T-matrix operator to obtain the scattering coefficients to obtain the electric and magnetic fields at every point in space. From this, we can obtain the scattered power $P = \frac{1}{2} \int_{\Omega} \text{Re}(\vec{E} \times \vec{H}^*) \cdot d\vec{A}$. We excite our structure with two octupole modes and two hexadecapole modes chosen so that one maximizes the amount of mode mixing and one minimizes the amount of mode mixing and plot the scattered power of each excited mode below.

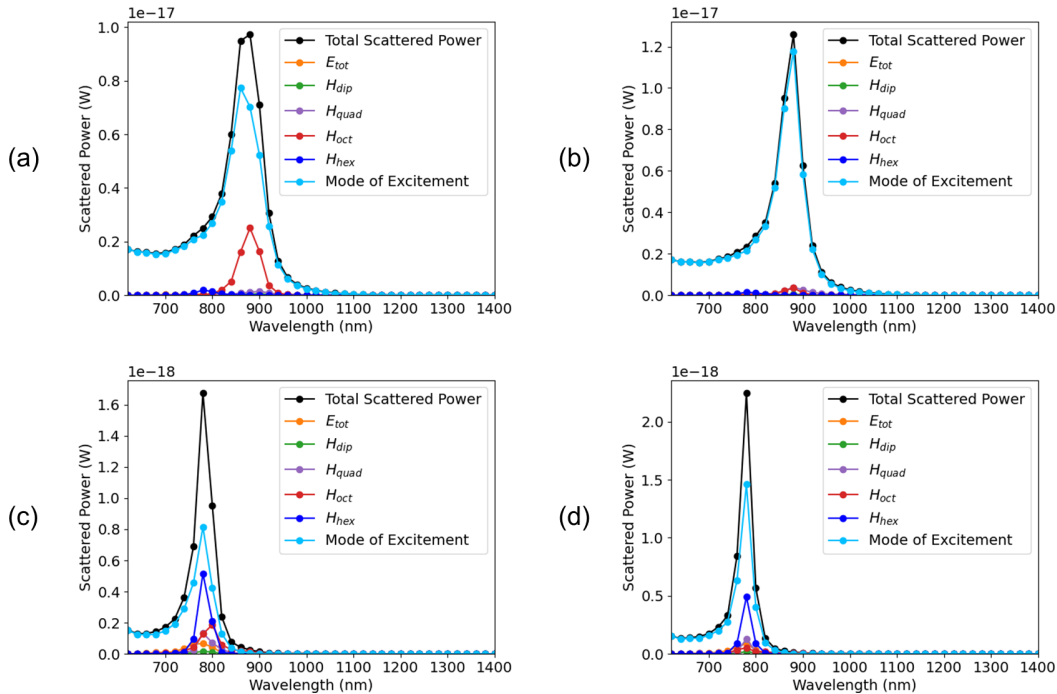


Figure 10: The modal scattered power for single mode excitation. The exciting mode chosen in each case was (a) the incident magnetic octupole mode that maximizes and (b) the incident magnetic octupole mode that minimizes the scattered power that comes from modes other than the exciting mode, respectively. The exciting modes chosen for c and d are (c) the incident magnetic hexadecapole mode that maximizes and (d) the incident magnetic hexadecapole mode that minimizes the scattered power that comes from modes other than the exciting mode, respectively. The specific modes used are $(n, m) = (3, 2)$ for a, $(n, m) = (3, 0)$ for b, $(n, m) = (4, 3)$ for c, and $(n, m) = (4, 4)$ for d.

Now if mode mixing effects are not significant then we should expect that exciting a structure with one pure submode will result in only seeing scattered power from that particular submode as calculated from the formula above. For some submodes this is approximately the case (Figure 7b) but others show scattered power from various other modes (Figures 7a, c-d) indicating potent mode mixing effects. Thus if we completely disregarded mode mixing the scattering for the higher order modes would look drastically

different for single excitations. We see that higher order modes tend to mix more as even the lowest mixing hexadecapole mixes more than the highest mixing octupole. This explains why the diagonal T matrix underestimates the magnetic octupole and hexadecapole contributions (See Figure S12). We also see that there is great variation in how the submodes mix indicating a level of disorder which we also saw through the elaborate patterns in the higher order T matrices (Figure 8c-d). Moreover, as the mode order increases, we see the modes start to mix more with lower order modes and even some electric modes as seen by the large non hexadecapole contributions in Figure 7c-d.

Thus in summary, we have shown that mode mixing effects may be significant in large structures with higher order resonances. Though the effects on the total scattering may generally be small, these effects may need to be taken into consideration in experiments and simulations with more selective polarizations and in directional scattering experiments.

Angular Scattering of Higher Order Magnetic Modes

One large issue with experimental results is that since the features tend to be significantly broadened due to heterogeneity of DMMS in solution ensembles, it becomes quite difficult to characterize them as we have seen earlier and as discussed in previous experimental studies¹². As we will show, it may be significantly easier to characterize them using directional scattering methods. Each mode has a characteristic angular scattering pattern and these modes have recently been of interest due to their ability to superimpose resulting in constructive and destructive interference.²⁵ Below we show the backscattering of our 70nm bead structure for a full T-matrix as well as $|X_\phi^H|$, ReX_ϕ and ImX_ϕ in the backscattering direction to visualize the modal contributions. See Figure S13 for a full breakdown including $|X_\phi^E|$ and $Phase(X_\phi)$.

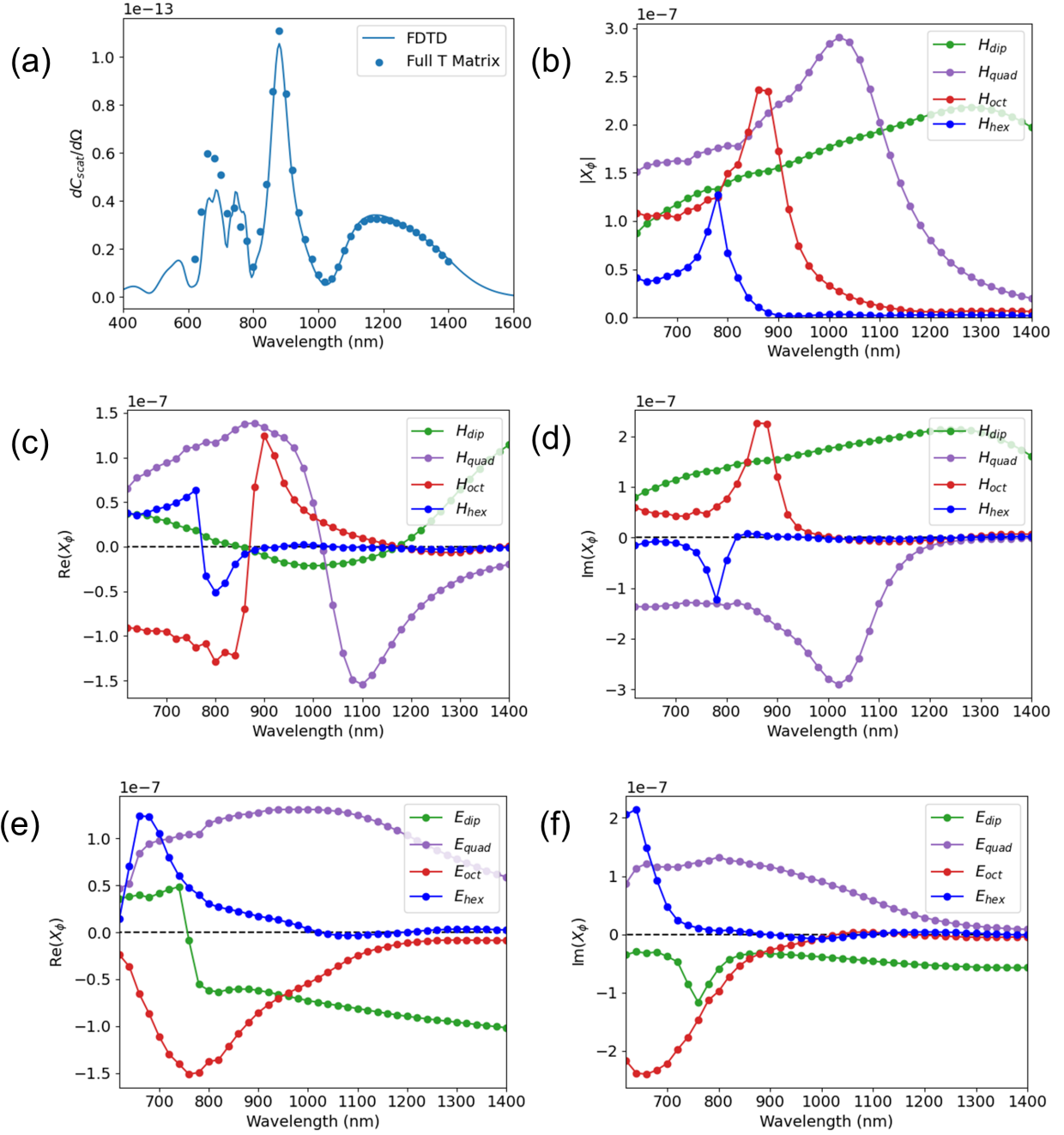


Figure 11: (a) Backscattering cross section for the FDTD and T-matrix of the $N = 126$, $D = 70$, $Z = 415$ MM and (b) $|X_\phi|$ of the magnetic modes. $\text{Re}(X_\phi)$ of the (c) magnetic and (e) electric modes and $\text{Im}(X_\phi)$ of the (d) magnetic and (f) electric modes. Note that \vec{X} has a θ component but is small compared to its ϕ component in the backscattering. For $|X_\phi|$ of the electric modes as well as the phase of both electric and magnetic modes see Figure S13

As we can see in Figure 11a, the full T matrix successfully predicts the major features of the backscattering starting from about $\lambda = 700$ nm onwards including the dips at 800 nm and 1020 nm and the peaks at 880 nm and 1200 nm. Notice the shape of the higher order magnetic modes $X_\phi^{H_Q}$, $X_\phi^{H_O}$, and $X_\phi^{H_H}$. We see

that the higher order magnetic modes of the beads resonate within a sharp wavelength band (Figure 11b) as explained before which gives us a high-Q resonance that takes a shape similar to that of a Lorentz oscillator (Figure 11c-d).¹⁹ The electric modes experience this to a much weaker extent in the wavelength range of interest (Figure S13c) and so they remain relatively constant over the wavelength range of interest (Figure 11e-f). This results in interference between the sharp higher order magnetic modes and the smooth electric modes leading to Fano-like resonant patterns in the differential scattering cross section. This overall makes the differential scattering look vastly different from the total scattering despite the overall resemblance seen in the amplitude plot (Figure 11b).

In principle, we can use this selective directional scattering and modal interference to visualize scattering modes that are weak in the total scattering. We saw earlier in Figure 5 that the magnetic quadrupole and magnetic dipole interfered to enhance their forward scattering and effectively cancel out their backscattering at the quadrupole resonance. We see in Figures 11c-d that around 1020 nm, the real part of the magnetic quadrupole passes through zero and its imaginary part entirely cancels with the magnetic dipole and electric quadrupole resulting in a dip in the backscattering at the 1020nm magnetic quadrupole resonance (Figure 11a). We see in Figure 11c-d and 11e-f that the other modes from 800 nm to 1000 nm are relatively constant and largely cancel each other out which allows the sharp magnetic octupole to be the dominant feature in the spectrum at this range. This octupole enhancement in the backscattering is advantageous as backscattering at this range is easily measured in experiments and so this can be used to visualize a far field magnetic octupole for the first time. We show example FDTD backscattering simulations for various structures in Figure 12 below.

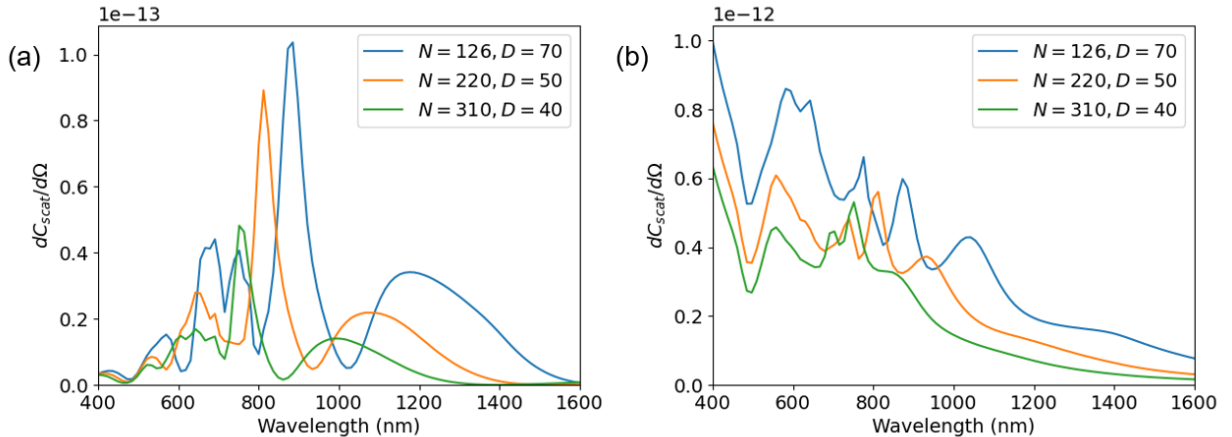


Figure 12: (a) FDTD Backscattering and (b) forward scattering cross section of a $Z = 415$ nm core with varying bead number and bead size. As can be seen, the general features remain highly conserved for a wide range of structural parameters as long as the core is sufficiently large.

From Figure 12a we observe that the octupole peak is much sharper than the peak we saw in the total scattering and so it is likely visible in experiments even with spectral broadening. Moreover, we can clearly see that this phenomena is not limited to just one specific structure but in fact holds even as we shrink the beads and increase the number of them which indicates that as long as the structure is large enough to support octupoles and the beads are packed enough, we should be able to observe them in single particle backscattering measurements regardless of specific bead configurations. Thus we can take advantage of modal interferences in the backscattering to observe far field magnetic octupoles for the first time.

Conclusion

In this paper we have used a T-matrix based approach to characterize the higher order magnetic modes of model MM systems including magnetic quadrupoles, octupoles, and hexadecapoles. We have used FDTD

simulations to compute the T-matrix to obtain the scattering contribution of each mode and we saw that as the structure grows in size the higher order magnetic modes become the dominant scattering modes. We also saw that as higher order modes become dominant, mixing becomes visible in the scattering cross section. Though this effect is small, we found that it becomes significantly more pronounced in directional scattering and with selective polarizations that see higher contributions from higher order modes. We also proposed that this mode mixing can bring about or enhance chiral effects.

We then used our T-matrix method to obtain the vector scattering amplitude and differential scattering cross sections and saw that higher order magnetic modes behave as high Q resonators that interfere with other modes to produce Fano-like resonances in certain orientations. We used this knowledge to propose an experiment using backscattering analysis that could be used to visualize magnetic octupoles in the far field for the first time. Figuring out a way to tune these mode mixing terms and angular resonances would allow for extremely high flexibility in using MMs to design materials with unique optical properties.

References

- (1) Calandrini, E.; Cerea, A.; Angelis, F. D.; Zaccaria, R. P.; Toma, A. Magnetic hot-spot generation at optical frequencies: from plasmonic metamolecules to all-dielectric nanoclusters. *Nanophotonics* **01 Jan. 2019**, *8*, 45 – 62.
- (2) Monticone, F.; Alù, A. The quest for optical magnetism: from split-ring resonators to plasmonic nanoparticles and nanoclusters. *J. Mater. Chem. C* **2014**, *2*, 9059–9072.
- (3) Ha, M.; Kim, J.-H.; You, M.; Li, Q.; Fan, C.; Nam, J.-M. Multicomponent Plasmonic Nanoparticles: From Heterostructured Nanoparticles to Colloidal Composite Nanostructures. *Chemical Reviews* **2019**, *119*, 12208–12278, PMID: 31794202.
- (4) Liberal, I.; Engheta, N. Near-zero refractive index photonics. *Nature Photonics* **2017**, *11*, 149–158.
- (5) Ramakrishna, S. Physics of negative refractive index materials. *Reports on Progress in Physics* **2005**, *68*, 449–521.
- (6) Padilla, W. J.; Basov, D. N.; Smith, D. R. Negative refractive index metamaterials. *Materials Today* **2006**, *9*, 28 – 35.
- (7) Cai, W.; Chettiar, U.; Kildishev, A.; Shalaev, V. Optical Cloaking with Non-Magnetic Metamaterials. **2006**, *1*, 224–227.
- (8) Zambrana-Puyalto, X.; Bonod, N. Tailoring the chirality of light emission with spherical Si-based antennas. *Nanoscale* **2016**, *8*, 10441–10452.
- (9) Chen, J.; Fan, W.; Zhang, T.; Tang, C.; Chen, X.; Wu, J.; Li, D.; Yu, Y. Engineering the magnetic plasmon resonances of metamaterials for high-quality sensing. *Optics Express* **2017**, *25*, 3675–3681.
- (10) Fang, N.; Lee, H.; Sun, C.; Zhang, X. Sub-Diffraction-Limited Optical Imaging with a Silver Superlens. *Science* **2005**, *308*, 534–537.
- (11) Qian, Z.; Hastings, S. P.; Li, C.; Edward, B.; McGinn, C. K.; Engheta, N.; Fakhraai, Z.; Park, S.-J. Raspberry-like Metamolecules Exhibiting Strong Magnetic Resonances. *ACS Nano* **2015**, *9*, 1263–1270, PMID: 25621502.
- (12) Lee, S.; Woods, C. N.; Ibrahim, O.; Kim, S. W.; Pyun, S. B.; Cho, E. C.; Fakhraai, Z.; Park, S.-J. Distinct Optical Magnetism in Gold and Silver Probed by Dynamic Metamolecules. *The Journal of Physical Chemistry C* **2020**, *124*, 20436–20444.
- (13) Manna, U.; Lee, J.-H.; Deng, T.-S.; Parker, J.; Shepherd, N.; Weizmann, Y.; Scherer, N. F. Selective Induction of Optical Magnetism. *Nano Letters* **2017**, *17*, 7196–7206, PMID: 29111760.

- (14) Bakhti, S.; Tishchenko, A. V.; Zambrana-Puyalto, X.; Bonod, N.; Dhuey, S. D.; Schuck, P. J.; Cabrini, S.; Alayoglu, S.; Destouches, N. Fano-like resonance emerging from magnetic and electric plasmon mode coupling in small arrays of gold particles. *Scientific Reports* **2016**, *6*.
- (15) Parker, J.; Gray, S.; Scherer, N. F. Optical magnetism in core-satellite nanostructures excited by vector beams. Photonic and Phononic Properties of Engineered Nanostructures VIII. 2018; pp 60 – 68.
- (16) Parker, J.; Gray, S.; Scherer, N. Multipolar analysis of electric and magnetic modes excited by vector beams in core-satellite nano-structures. 2017.
- (17) Hastings, S. P.; Qian, Z.; Swanglap, P.; Fang, Y.; Engheta, N.; Park, S.-J.; Link, S.; Fakhraai, Z. Modal interference in spiky nanoshells. *Opt. Express* **2015**, *23*, 11290–11311.
- (18) Haynes, W. M. *CRC Handbook of Chemistry and Physics*, 95th ed.; CRC Press: USA, 2014.
- (19) *Absorption and Scattering of Light by Small Particles*; John Wiley & Sons, Ltd, 1998.
- (20) Hastings, S. P. The Optical Properties of Spiky Gold Nanoshells. Ph.D. thesis, University of Pennsylvania, 2014.
- (21) *Scattering of Electromagnetic Waves: Theories and Applications*; John Wiley & Sons, Ltd, 2000.
- (22) Alù, A.; Salandrino, A.; Engheta, N. Negative effective permeability and left-handed materials at optical frequencies. *Opt. Express* **2006**, *14*, 1557–1567.
- (23) Alù, A.; Engheta, N. Dynamical theory of artificial optical magnetism produced by rings of plasmonic nanoparticles. *Phys. Rev. B* **2008**, *78*, 085112.
- (24) Li, C.; Lee, S.; Qian, Z.; Woods, C.; Park, S.-J.; Fakhraai, Z. Controlling Magnetic Dipole Resonance in Raspberry-like Metamolecules. *The Journal of Physical Chemistry C* **2018**, *122*, 6808–6817.
- (25) Deng, T.-S.; Parker, J.; Hirai, Y.; Shepherd, N.; Yabu, H.; Scherer, N. F. Designing "Metamolecules" for Photonic Function: Reduced Backscattering. *physica status solidi (b)* **2020**, *257*, 2000169.
- (26) Virtanen, P. et al. SciPy 1.0: Fundamental Algorithms for Scientific Computing in Python. *Nature Methods* **2020**, *17*, 261–272.

Acknowledgement

S.-J.P. acknowledges the financial support from the National Research Foundation (NRF) of Korea (NRF-2018R1A2B3001049) and the Science Research Center (SRC) funded by NRF (NRF-2017R1A5A1015365). Z.F., C.N.W., and O.I. acknowledge funding from the Penn Laboratory for Research in Structure of Matter (LRSM) funded by NSF MRSEC grant (DMR-1720530), the Department of Chemistry (summer fellowship for O.I.), and the School of Arts and Sciences Dean’s Global Inquiries Fund at the University of Pennsylvania (Funded visit to South Korea for C.N.W.). C.N.W. was supported by a fellowship from the REACT for the Human Habitats Program at Penn (through NSF PIRE Grant #OISE-1545884).

Supporting Information Available

I. Additional Simulation Details

In theory the \vec{E} and \vec{H} fields of the entire volume can be saved but this would be highly space inefficient, making T-matrix analysis slow or expensive. To address this, we recursively broke the mesh region of the FDTD simulations into octants with a cube monitor placed at each octant location that contains a mesh point within $r = [R_{int} - \frac{\sqrt{3}}{2}dx, R_{int} + \frac{\sqrt{3}}{2}dx]$ (where R_{int} is the radius of integration and dx is the maximum mesh step). This ensures that there is always a cube of data points around each point on the integration sphere for grid interpolation. This cuts the volume of data saved by a factor of up to 10 depending on the recursion depth used. These cubic monitors were then iteratively merged to form rectangular prisms in order to reduce the number of data files saved.

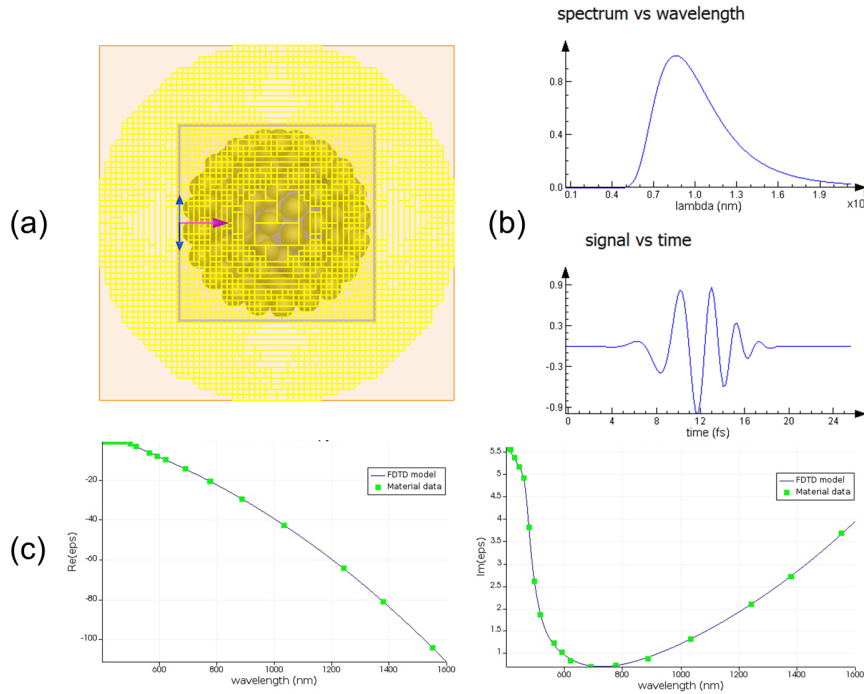


Figure S1: Details of (a) the T-Matrix simulation including simulation setup, (b) the plane wave pulse used to excite the particle, and (c) the material fit used for the gold NPs based on the CRC Handbook optical data¹⁸

The setup for the T matrix is shown in Figure S1a. Two meshes were used: a fine mesh (with a 2.5nm mesh size) encapsulating both the MM and the plane wave source (both inside the grey box) and a coarse mesh (with a 5nm mesh size) on the outside where the scattered field was collected (outer orange box). The yellow shell made of rectangular monitors can be seen above in the region within the outer mesh but outside the inner mesh.

II. Calculation of the T-Matrix

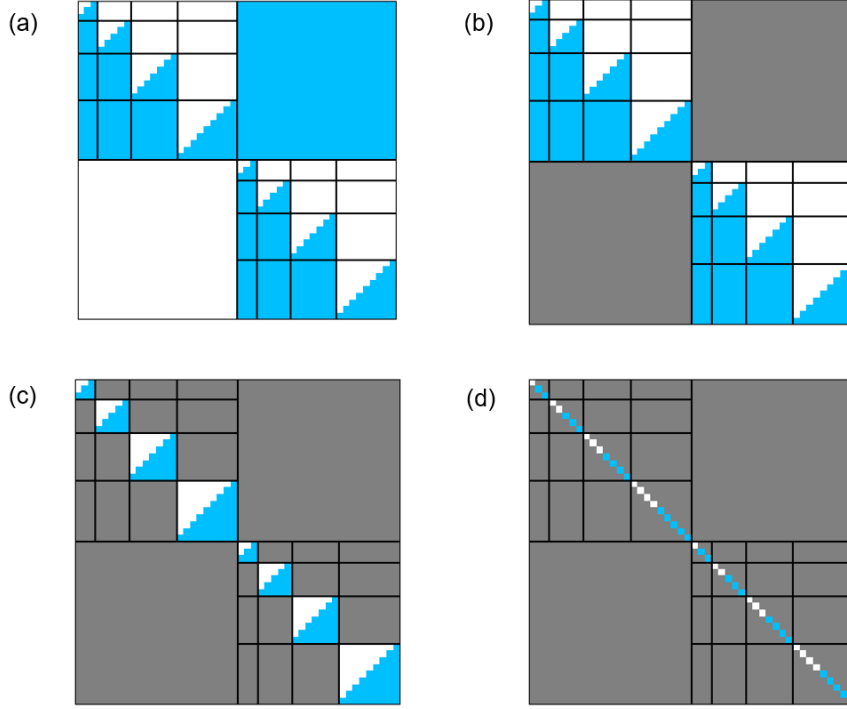


Figure S2: A possible set of free fit parameters for (a) the full T matrix, (b) the block diagonal T matrix, (c) the IMM T matrix, and (d) the diagonal T matrix with a maximum n of 4. Note that a blue square is an independent element, a white square is a dependent element, and a grey square is fixed at 0

As stated previously, we take advantage of the T matrix reciprocity relation $T_{-m'n'(-m)n}^{ij} = (-1)^{m'+m} T_{mnm'n'}^{ji}$ for $i, j = \{E, M\}$ in order to reduce the number of free fit parameters for the T matrix.²¹ Above we show a set of free fit parameters for each type of T matrix that we minimize over. To compute the T-matrix from the above expression we do a minimization over the T-matrix elements using the scipy library for Python. In particular, we use the function `scipy.optimize.minimize` (using the SLSQP solver).²⁶

III. Obtaining Optical Properties from the T Matrix

Once we have obtained the T-matrix at a given frequency we can use it to determine the scattering cross section C_{scat} for any incident direction, the differential scattering cross section $\frac{dC_{scat}}{d\Omega}$ for any given incident and scattering direction, and the vector scattering amplitude \vec{X} for any incident and scattering direction. We can also obtain the far field scattered electric field $\vec{E}_s(\theta, \phi)$ and far field displacement current $\vec{J}_D(\theta, \phi)$. All these computations hinge on being able to determine the far field scattering amplitude dyad $\overline{\overline{F}}$. In the far field limit the scattering amplitude dyad $\overline{\overline{F}}$ is related to the scattered electric field by the relation:

$$\vec{E}_s(\vec{r}) = \frac{e^{ikr}}{r} \overline{\overline{F}}(\theta_s, \phi_s, \theta_i, \phi_i) \cdot \hat{\beta} E_0 \quad (8)$$

where (θ_s, ϕ_s) represents the direction of scattered light, (θ_i, ϕ_i) represents the direction of incident light, $\hat{\beta}$ is the unit polarization vector, and E_0 is the amplitude. We can obtain $\overline{\overline{F}}$ from the T-matrix as follows:

$$\begin{aligned} \overline{\overline{F}}(\theta_s, \phi_s, \theta_i, \phi_i) = & \frac{4\pi}{k} \sum_{n,m,n',m'} (-1)^{m'} i^{n'-n-1} * \{ [T_{mnm'n'}^{EE} i \gamma_{mn} \overline{B}_{mn}(\theta_s, \phi_s) + T_{mnm'n'}^{EM} \gamma_{mn} \overline{C}_{mn}(\theta_s, \phi_s)] \\ & \cdot \gamma_{-m'n'} \frac{\overline{B}_{-m'n'}(\theta_i, \phi_i)}{i} + [T_{mnm'n'}^{MM} \gamma_{mn} \overline{C}_{mn}(\theta_s, \phi_s) + T_{mnm'n'}^{ME} i \gamma_{mn} \overline{B}_{mn}(\theta_s, \phi_s)] \cdot \gamma_{-m'n'} \overline{C}_{-m'n'}(\theta_i, \phi_i) \} \end{aligned} \quad (9)$$

In this equation $\overline{B}_{mn}(\theta, \phi)$ and $\overline{C}_{mn}(\theta, \phi)$ are the two vector spherical harmonics that satisfy the vector wave equation. Using $\overline{\overline{F}}$ we can obtain the vector scattering amplitude $\vec{X}(\theta_s, \phi_s) = \overline{\overline{F}}(\theta_s, \phi_s, \theta_i, \phi_i) \cdot \hat{e}_i$. From \vec{X} we can easily obtain the differential scattering cross section in the (θ_s, ϕ_s) direction $\frac{dC_{scat}}{d\Omega} = |\vec{X}(\theta_s, \phi_s)|^2$ and the scattering cross section $C_{scat}(\theta_i, \phi_i) = \int_{4\pi} d\Omega [|\overline{\overline{F}}(\theta, \phi, \theta_i, \phi_i) \cdot \hat{\beta}|^2]$.²⁰ Note that instead of numerical integration we instead use an exact formula:^{19,21}

$$\begin{aligned} C_{scat}(\theta_i, \phi_i) = & \frac{16\pi^2}{k^2} \sum_{n,m} \{ | \sum_{m',n'} i^{n'} (-1)^{m'} \gamma_{-m'n'} [T_{mnm'n'}^{EE} \frac{\overline{B}_{-m'n'}(\theta_i, \phi_i)}{i} \cdot \hat{\beta} + T_{mnm'n'}^{EM} \overline{C}_{-m'n'}(\theta_i, \phi_i) \cdot \hat{\beta}]|^2 + \\ & | \sum_{m',n'} i^{n'} (-1)^{m'} \gamma_{-m'n'} [T_{mnm'n'}^{MM} \overline{C}_{-m'n'}(\theta_i, \phi_i) \cdot \hat{\beta} + T_{mnm'n'}^{ME} \frac{\overline{B}_{-m'n'}(\theta_i, \phi_i)}{i} \cdot \hat{\beta}]|^2 \} \end{aligned} \quad (10)$$

Notice that the formulas for scattering cross section C_{scat} and $\overline{\overline{F}}$ are linear in the scattering mode n and so we can obtain the exact modal contributions to C_{scat} , \vec{E}_s , and \vec{J}_D which is useful in our analysis. Now we use the T-matrix data to obtain far field displacement current maps which we can use to get a sense of the displacement currents of our structure. We know that in the far-field $\vec{E}_s(\vec{r}) = \frac{e^{ikr}}{r} \overline{\overline{F}}(\theta_s, \phi_s, \theta_i, \phi_i) \cdot \hat{e}_i E_0$. We know that in a linear medium, $\vec{J}_D = \epsilon_0 \frac{d\vec{E}}{dt} + \frac{d\vec{P}}{dt}$. Assuming a constant ϵ_r over the frequency range of interest we have $\vec{J}_D(\vec{r}, t) \propto \frac{d\vec{E}(\vec{r}, t)}{dt}$. Thus it follows that in the frequency domain we have $\vec{J}_D(\omega, \vec{r}) \propto -i\omega \vec{E}(\omega, \vec{r})$. Thus we can obtain \vec{J}_D from the T-matrix by computing \vec{E}_s . To produce a periodic animation from this we can convert the complex \vec{J}_D vector field to the standard basis and then obtain the amplitude (J_x, J_y, J_z) and phase $(\theta_x, \theta_y, \theta_z)$ in each direction. We then produce a 3D quiver plot of $\langle J_x \sin(\omega t - \theta_x), J_y \sin(\omega t - \theta_y), J_z \sin(\omega t - \theta_z) \rangle$ at a fixed value of r in the far-field at various points in time to produce a full animation.

This is also very useful in that the contributions of each mode to $\overline{\overline{F}}$ are linear in the mode n and so the cumulative displacement current $\vec{J}_D(\omega, \vec{r})$ is additive over all modes, meaning if we take the amplitudes and phase from each mode and superimpose all those waves we recover the total current. Note that this follows from the fact that for two complex numbers $z_1 = a_1 + b_1 i$ and $z_2 = a_2 + b_2 i$ we have that $\sqrt{(a_1 + a_2)^2 + (b_1 + b_2)^2} \sin(\omega t - \text{atan2}(b_1 + b_2, a_1 + a_2)) = \sqrt{a_1^2 + b_1^2} \sin(\omega t - \text{atan2}(b_1, a_1)) + \sqrt{a_2^2 + b_2^2} \sin(\omega t - \text{atan2}(b_2, a_2))$, which can be verified using a symbolic calculator. This allows us to analyze the modal contributions in an extremely useful way.

IV. Structural Parameters and Full FDTD Data for Model MMs

Table S1: Structural parameters for simulated gold MMs

Bead Number, N	Core Size, Z (nm)	Bead Size, D (nm)	Mean NN Distance, d_{avg} (nm)	Min NN Distance, d_{min} (nm)
126	360	60	66.87 ± 1.53	63.04
126	380	60	70.05 ± 1.61	66.04
126	400	60	73.24 ± 1.68	69.05
126	435	60	78.81 ± 1.81	74.30
126	215	35	39.80 ± 0.91	37.52
126	300	50	55.73 ± 1.28	52.54
126	415	70	77.22 ± 1.77	72.80
160	415	60	67.38 ± 1.56	63.67
220	415	50	56.29 ± 1.43	53.07
310	415	40	46.36 ± 1.13	43.47

Core Size Varying Series:

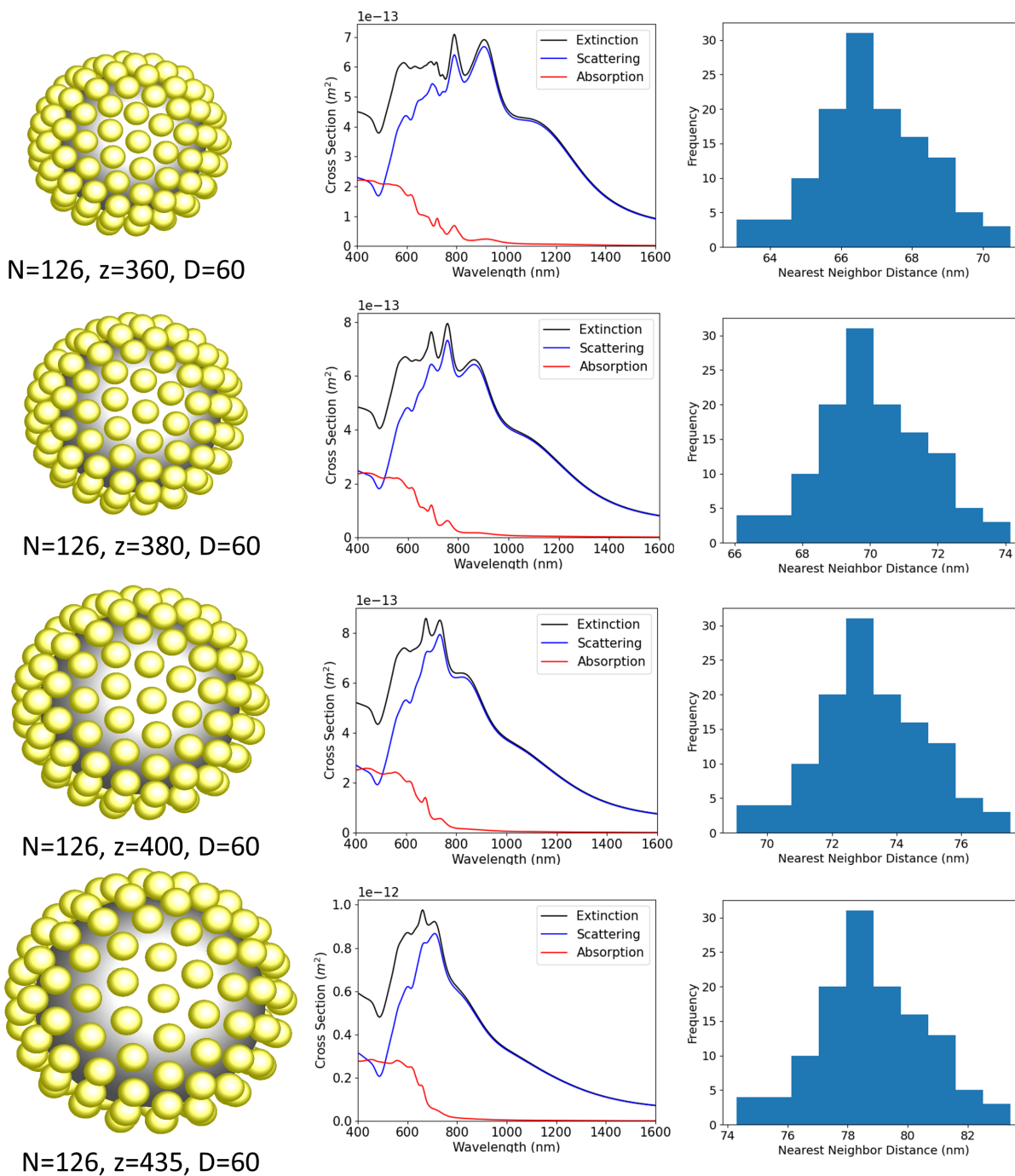


Figure S3: FDTD simulation results and nearest neighbor interparticle distance (d) histograms for the series where we vary Z .

Scaling Structure Series:

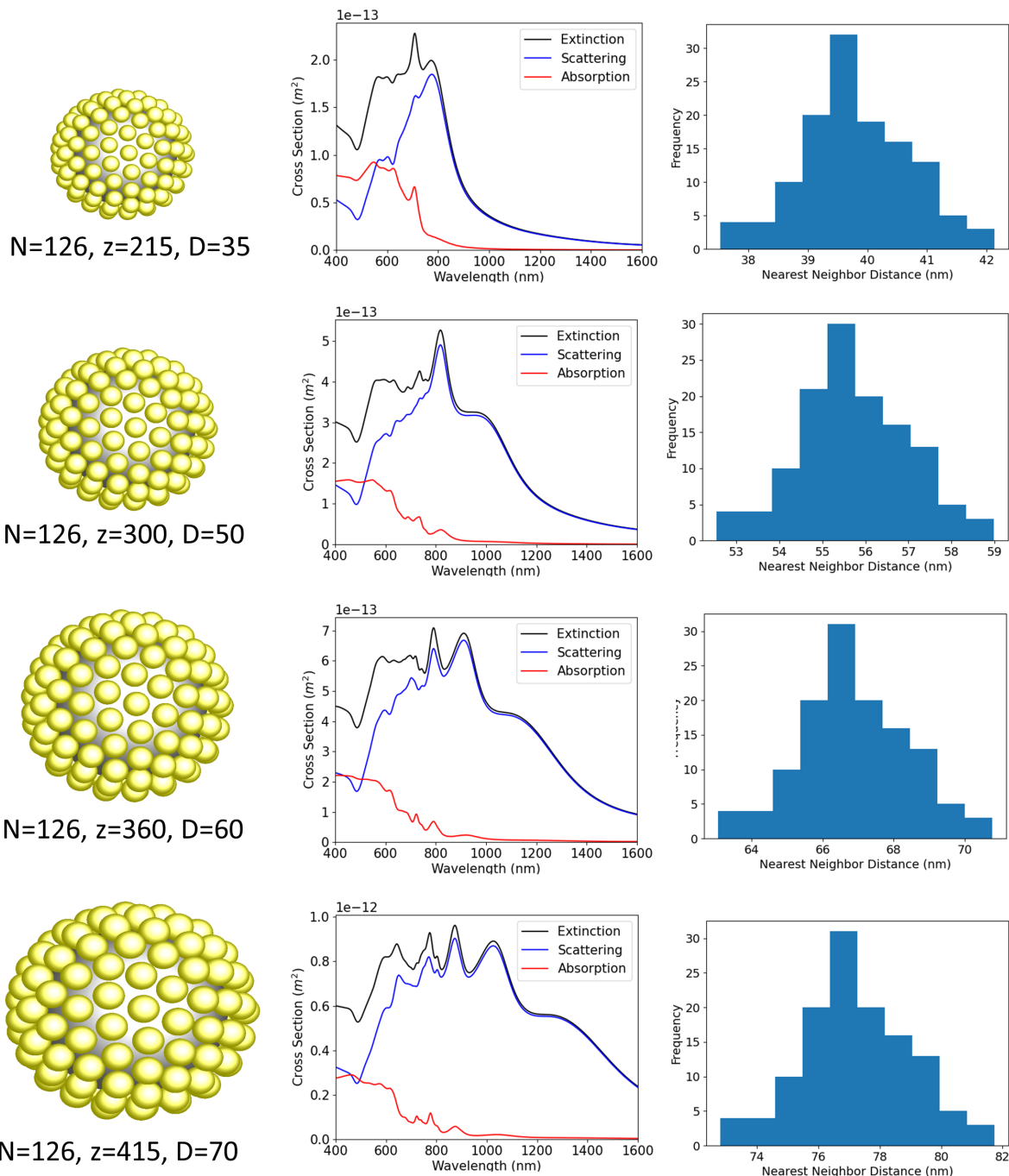


Figure S4: FDTD simulation results and nearest neighbor interparticle distance (d) histograms for the series where we keep the packing constant while varying Z and D .

Varying Bead Size/Number Series:

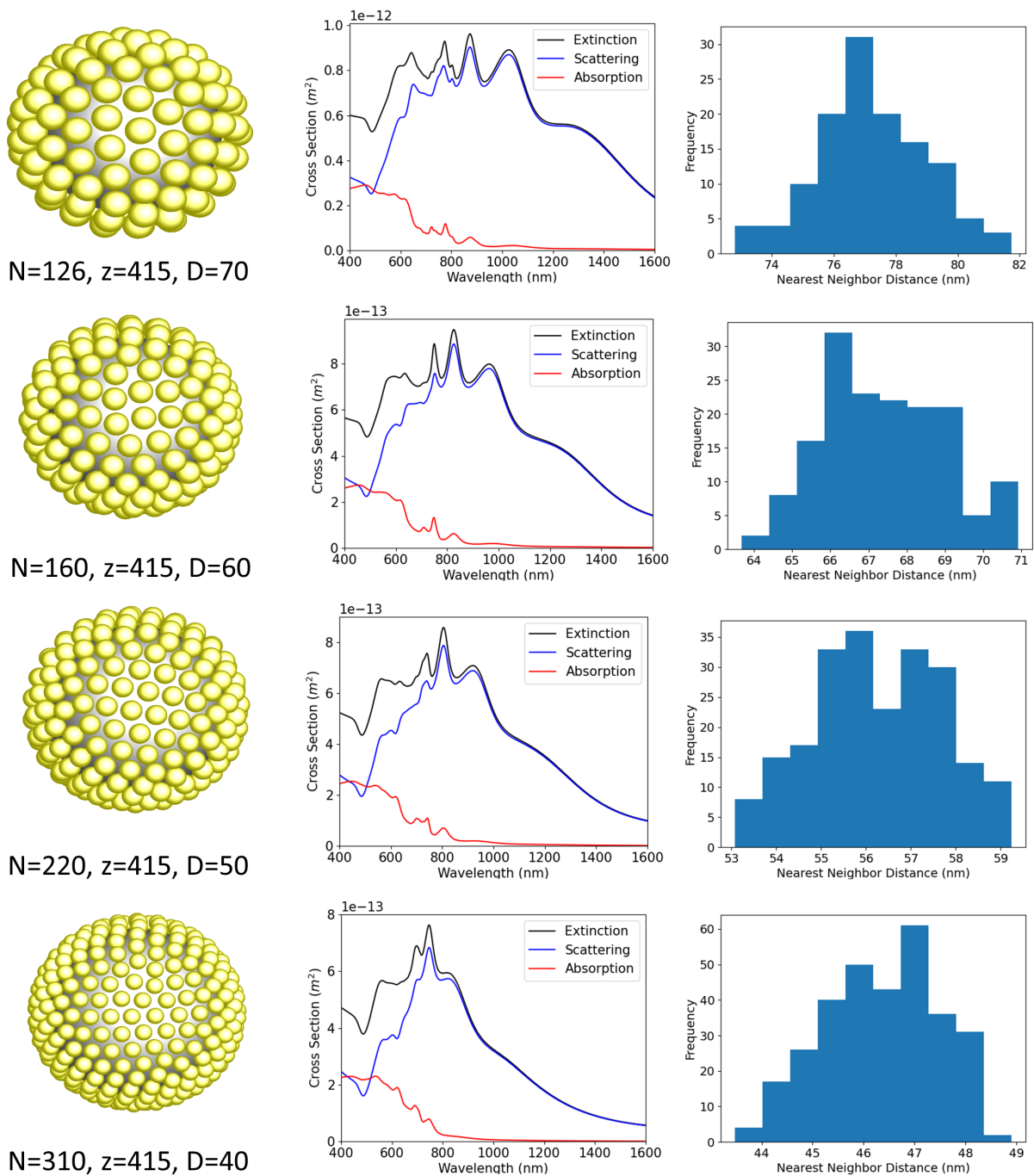


Figure S5: FDTD simulation results and nearest neighbor interparticle distance (d) histograms for the series where we keep Z constant while increasing N and decreasing D .

V. Full Modal Breakdown for Model MMs

Varying Core Size Series:

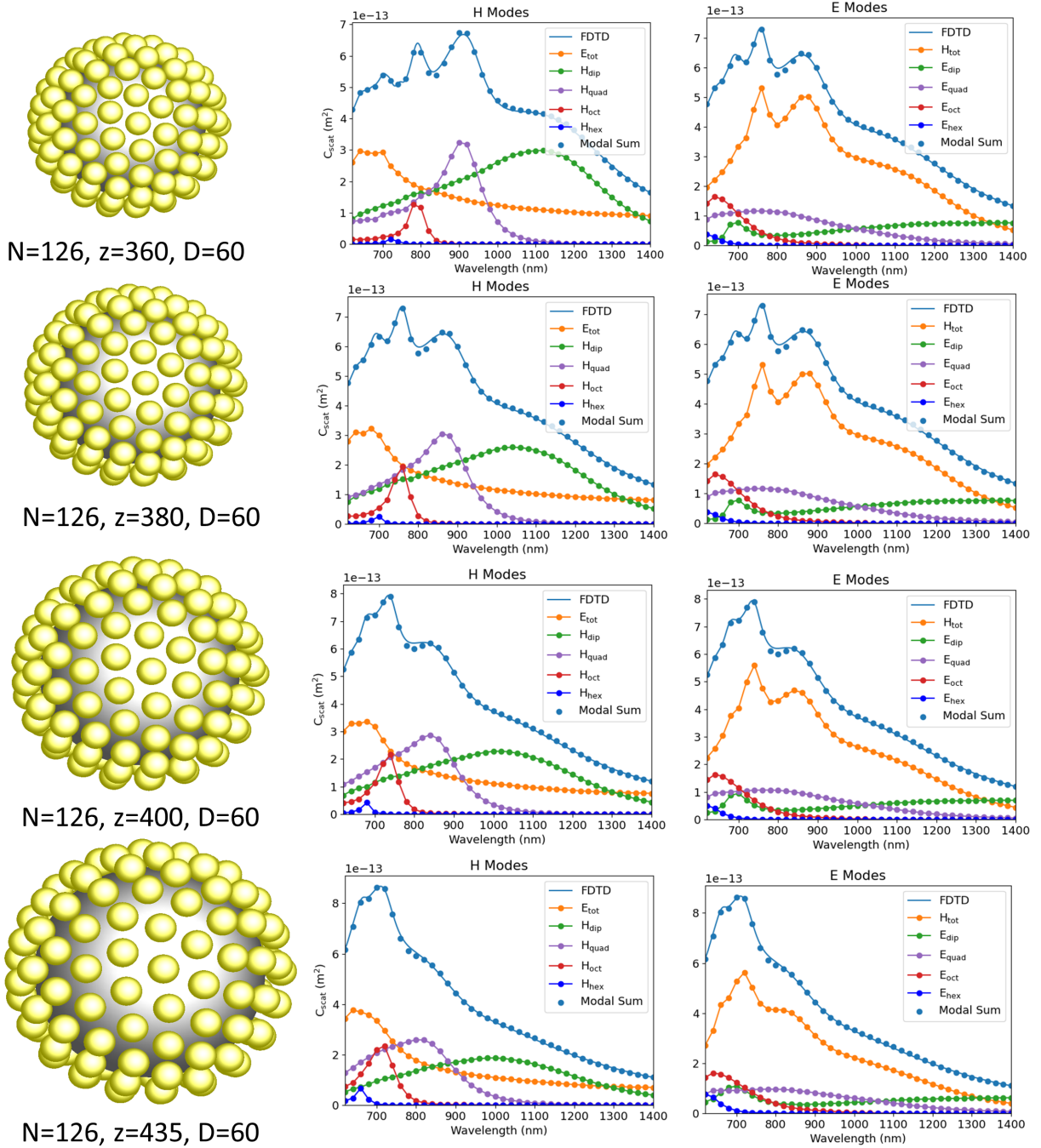


Figure S6: Full modal breakdown (including all electric and magnetic modal scattering cross sections) for the series where we vary Z .

Scaling Structure Series:

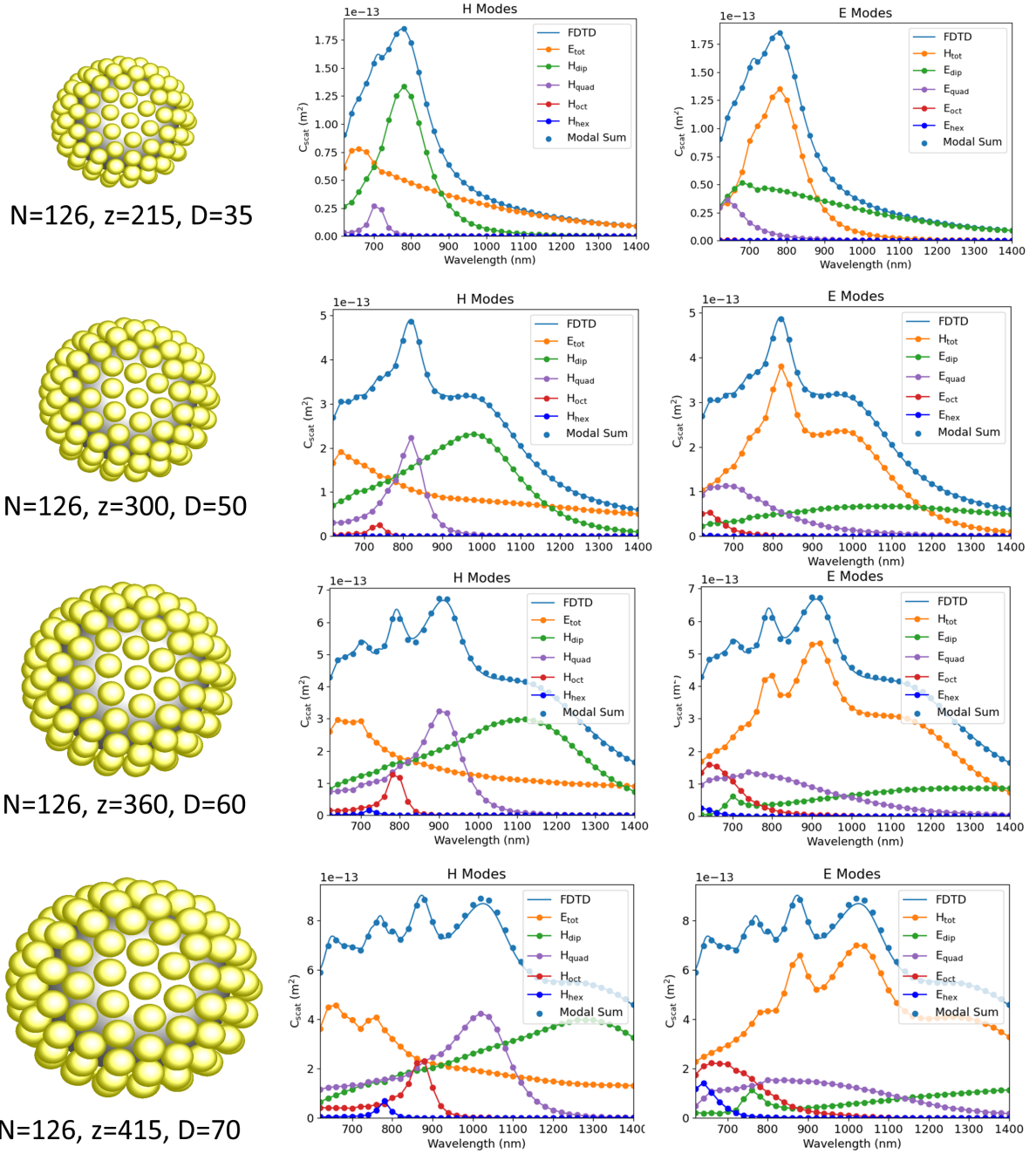


Figure S7: Full modal breakdown (including all electric and magnetic modal scattering cross sections) for the series where we keep the packing constant while varying Z and D .

Varying Bead Size/Number Series:

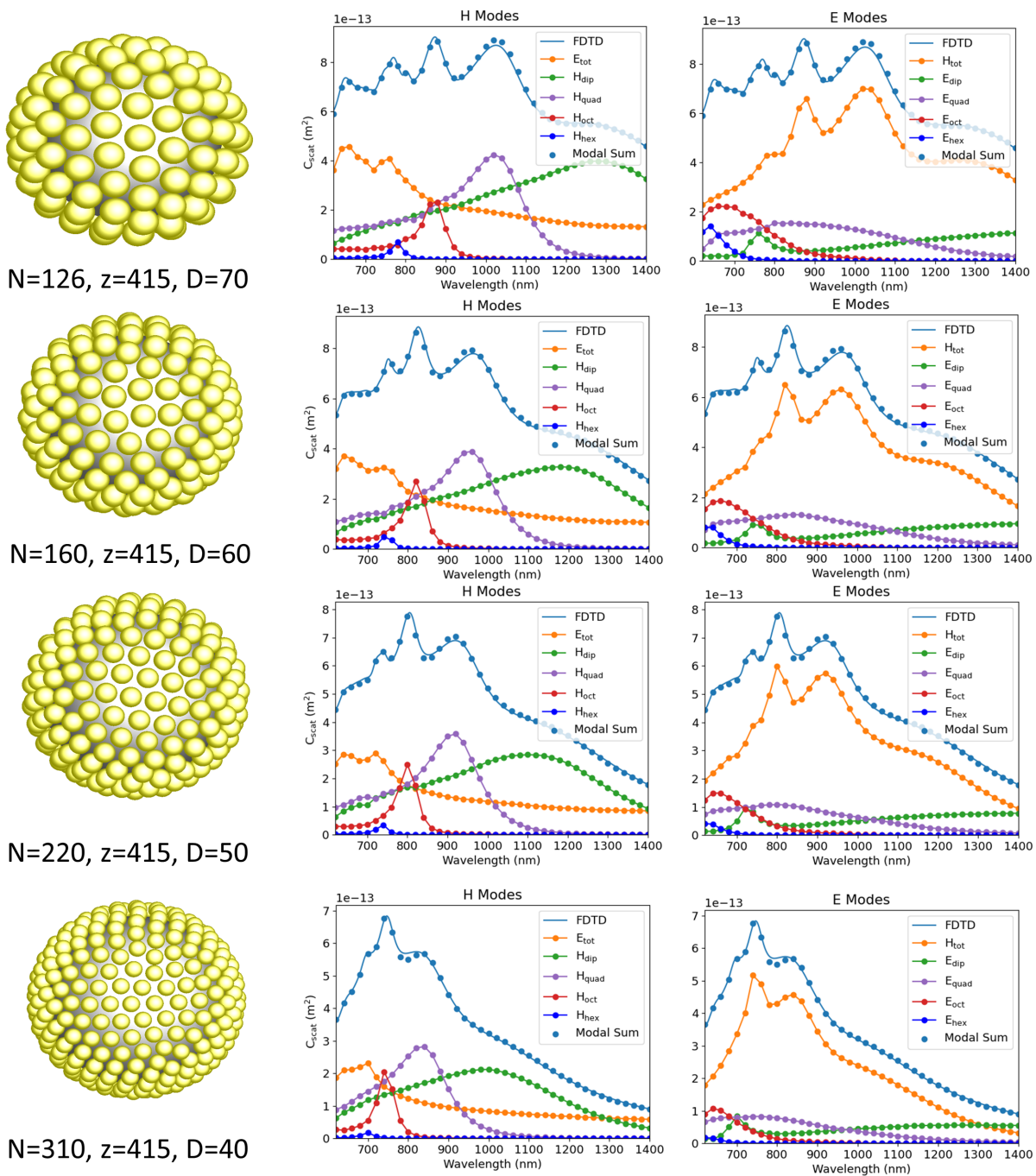
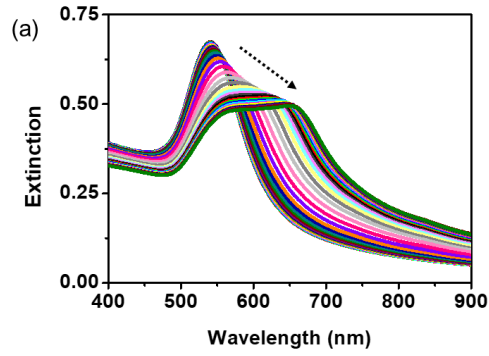


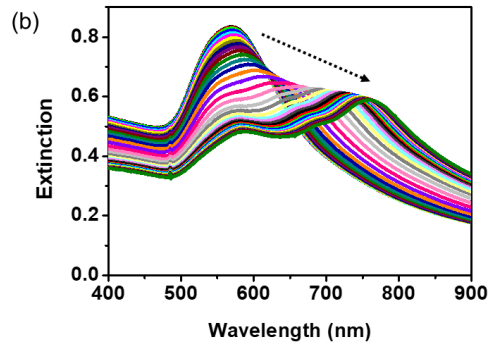
Figure S8: Full modal breakdown (including all electric and magnetic modal scattering cross sections) for the series where we keep Z constant while increasing N and decreasing D .

VI. Experimental Details



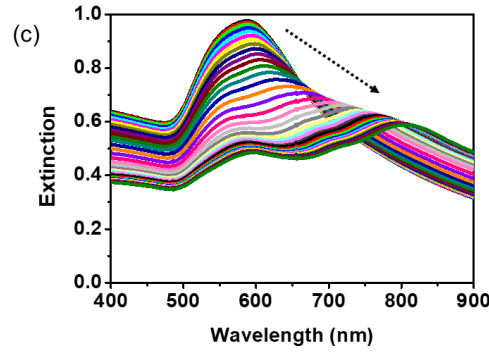
Peak Position

Temperature	Wavelength
20 °C	541 nm
25 °C	542 nm
50 °C	649 nm
55 °C	651 nm



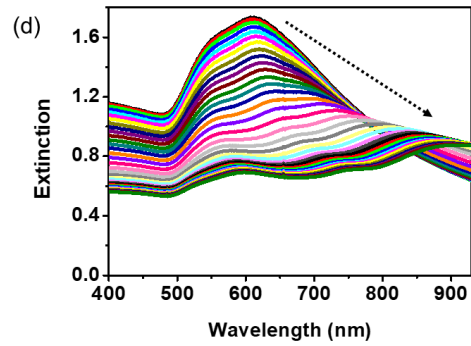
Peak Position

Temperature	Wavelength
20 °C	570 nm
25 °C	573 nm
50 °C	681 nm, 746 nm
55 °C	689 nm, 757 nm



Peak Position

Temperature	Wavelength
20 °C	588 nm
25 °C	591 nm
50 °C	705 nm, 789 nm
55 °C	714 nm, 801 nm



Peak Position

Temperature	Wavelength
20 °C	609 nm
25 °C	615 nm
50 °C	743 nm, 880 nm
55 °C	751 nm, 895 nm

Figure S9: Peak positions for experimental gold DMs of average number and size (a) $N = 57 \pm 3$, $D = 34.8 \pm 2.7$ nm, (b) $N = 61 \pm 4$, $D = 44.6 \pm 1.9$ nm (c) $N = 59 \pm 4$, $D = 49.2 \pm 2.4$ nm, and (d) $N = 41 \pm 4$, $D = 60.0 \pm 2.5$ nm.

Table S2: Experimental conditions and structural parameters for gold DMMs

	Bead Size (nm)	Concentration of Nanobead Solution (nM)	Number of Beads	Spectral Data
1	34.8 ± 2.7	0.2	57 ± 3	Figure 2a
2	44.6 ± 1.9	0.1	61 ± 4	Figure 2b
3	49.2 ± 2.4	0.1	59 ± 4	Figure 2c
4	60.0 ± 2.5	0.03	41 ± 4	Figure 2d

VII. Hexadecapole Current Data

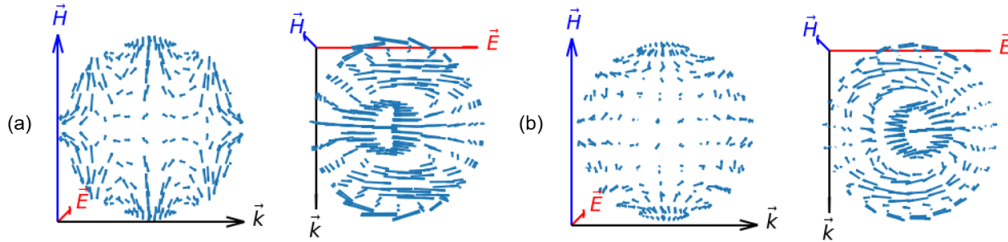


Figure S10: The far field displacement current plots of a pure (a) and mixed (b) hexadecapole at the hexadecapole resonance (780nm). The current maps are taken at the time that maximizes the sum of squared magnitude and are all scaled by the same constant value to highlight differences.

Above we show the hexadecapole current at the hexadecapole resonance (780nm) as calculated through a diagonal and a full T matrix at the point in time where the sum of square amplitudes is maximized. Note that this is scaled since the hexadecapole is quite weak (as seen in Figure 3).

Mode mixing has a profound effect on the hexadecapole. The field vectors throughout the structure begin to rotate and fall out of phase. Rather than resonating all at one point in time, the currents achieve their maximum amplitudes at different points in time resulting in current vectors that are weaker than the diagonal case which demonstrates the degree to which the currents fall out of phase.

VIII. Mie Based Explanation for MM Trends

As described before, the magnetic component of the incident electric field for a given mode and wavelength peaks at a certain distance from the center of the structure. The resonance narrows and blue shifts as the mode order increases and the resonance for all modes also broadens and red shifts as we move further from the center of the structure. When the beads fall within this resonant zone for a certain mode, the dipoles within the beads can resonate with the incident magnetic mode leading to strong magnetic scattering.

For a given n, m with a wave propagating in the z direction if we expand the electric field of the incident wave caused by the magnetic field in terms of spherical waves we get:²¹

$$E_H^{inc}(r, \theta, \phi) = - \sum_{n=1}^{\infty} \sum_{m=-n}^n i^n \frac{(2n+1)}{n(n+1)} \hat{e}_i \cdot \vec{C}_{-mn}(0, 0) j_n(kr) \vec{C}_{mn}(\theta, \phi) = - \sum_{n=1}^{\infty} j_n(kr) \sum_{m=-n}^n f_{mn}(\theta, \phi) \quad (11)$$

Thus we see that for a given mode and submode the radial strength of the incident mode depends only on $j_n(kr)$, a function of wavelength, refractive index of medium, and distance. For a diagonal T matrix the strength of the scattered mode is directly proportional to that of the incident mode and the proportionality constant is based on wavelength and structural parameters. We plot $j_n(kr)$ as a function of λ and r for

two different modes (dipole ($n = 1$) and octupole ($n = 3$)) and two different refractive indices ($N = 1$ and $N = 3$) below:

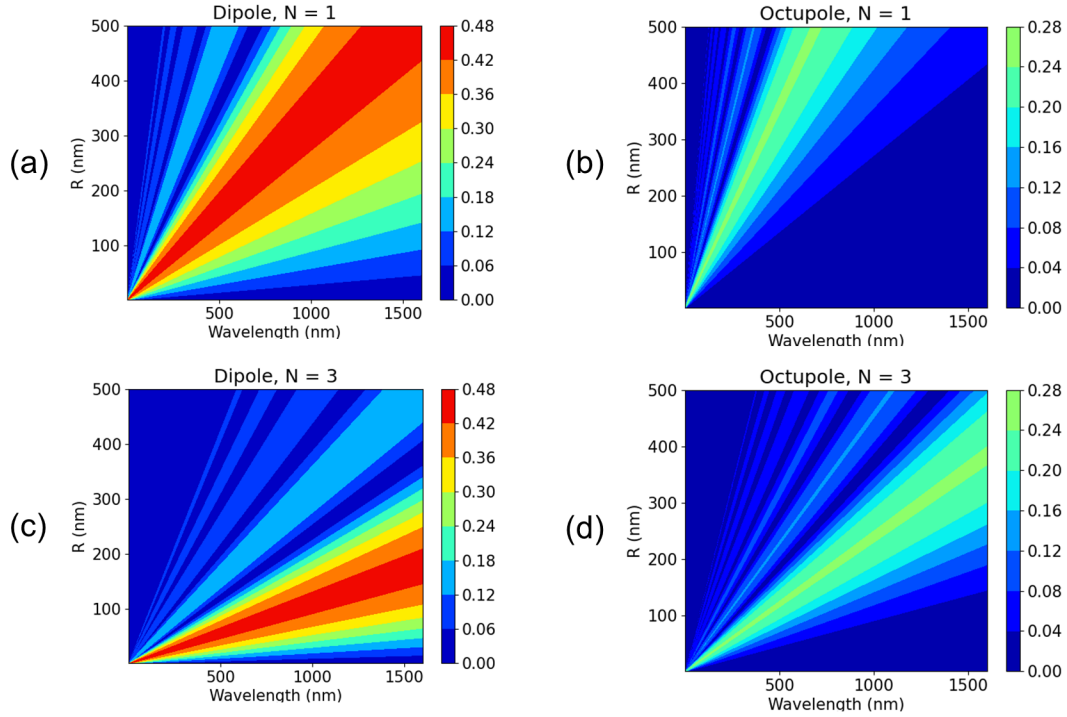


Figure S11: A plot of $j_n(kr)$ for (a) a magnetic dipole with $N = 1$, (b) a magnetic octupole with $N = 1$, (c) a magnetic dipole with $N = 3$, and (d) a magnetic octupole with $N = 3$. This represents the radial incident field strength of the magnetic component of the electric field of a plane wave.

We see that the higher order incident modes do not red shift as much as R increases which is consistent with the observation that higher order magnetic modes do not red shift as much as lower order modes as the structure is grown. Moreover, the width of the dipole incident peak at a fixed R is in general significantly larger than that of the octupole peak which may help explain why higher order modes tend to be sharper resonators. This also explains that as N grows for a fixed R (which is analogous to increasing the refractive index of the core), the wavelength of the resonance frequency increases while the width of resonance band increases and we can achieve stronger higher order modes with smaller structures which has been seen in previous studies.¹⁵ Thus we can explain many of our observations just by observing the nature of $j_n(kr)$.

IX. Diagonal T Matrix

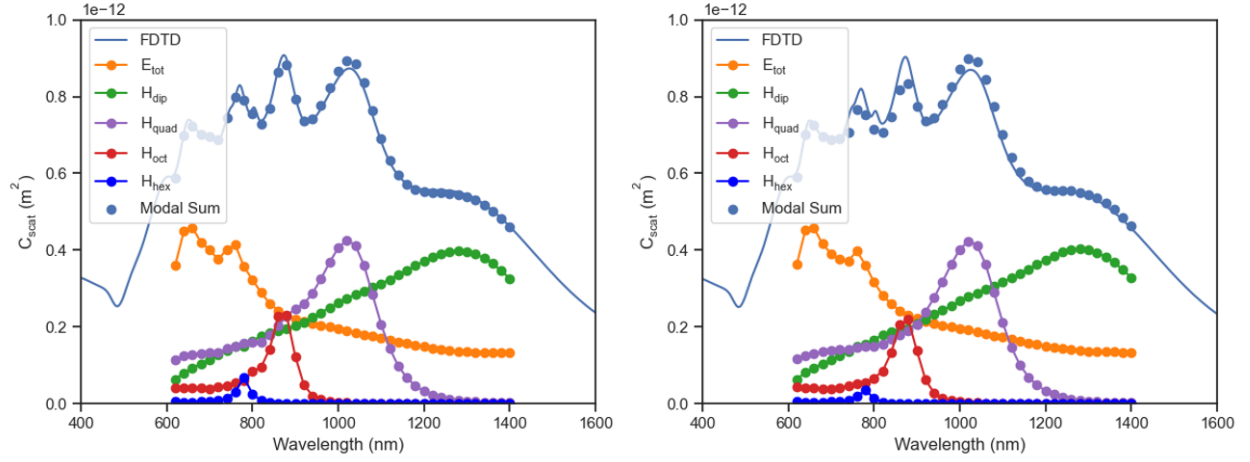


Figure S12: The modal scattering cross section obtained from the full T matrix (left) and diagonal T matrix (right) as well as the corresponding FDTD result.

Above we show side by side the scattering cross section obtained from the full T matrix (left) and the diagonal T matrix (right) and plot the FDTD result as well. We observe that the diagonal T matrix fit underestimates the contributions of both the magnetic octupole and the magnetic hexadecapole (as well as the quadrupole at the octupole peak) leading to significant error at these resonances.

X. Full Modal Breakdown of Backscattering

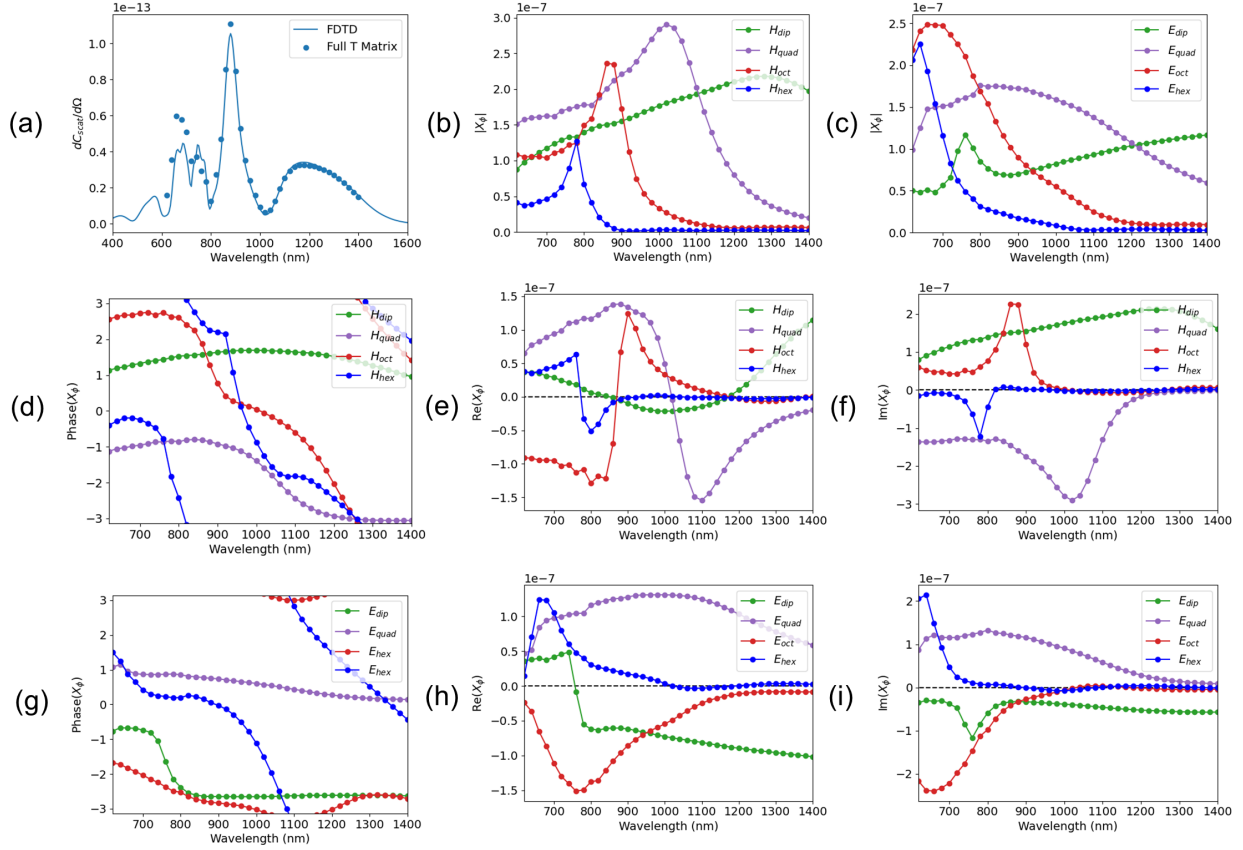


Figure S13: (a) Backscattering cross section for the FDTD and T-matrix of the 70nm bead MM. $|X_\phi|$ of the (b) magnetic and (c) electric modes. $\text{Phase}(X_\phi)$ of the (d) magnetic and (g) electric modes. $\text{Re}(X_\phi)$ of the (e) magnetic and (h) electric modes. $\text{Im}(X_\phi)$ of the (f) magnetic and (i) electric modes. Note that \vec{X} has a θ component but is small compared to its ϕ component for the backscattering.